



Population and individual firing behaviors in sparsely synchronized rhythms in the hippocampal dentate gyrus

Sang-Yoon Kim¹ · Woochang Lim¹

Received: 2 June 2021 / Revised: 26 September 2021 / Accepted: 2 October 2021
© The Author(s), under exclusive licence to Springer Nature B.V. 2021

Abstract

We investigate population and individual firing behaviors in sparsely synchronized rhythms (SSRs) in a spiking neural network of the hippocampal dentate gyrus (DG). The main encoding granule cells (GCs) are grouped into lamellar clusters. In each GC cluster, there is one inhibitory (I) basket cell (BC) along with excitatory (E) GCs, and they form the E-I loop. Winner-take-all competition, leading to sparse activation of the GCs, occurs in each GC cluster. Such sparsity has been thought to enhance pattern separation performed in the DG. During the winner-take-all competition, SSRs are found to appear in each population of the GCs and the BCs through interaction of excitation of the GCs with inhibition of the BCs. Sparsely synchronized spiking stripes appear successively with the population frequency $f_p (= 13.1 \text{ Hz})$ in the raster plots of spikes. We also note that excitatory hilar mossy cells (MCs) control the firing activity of the GC-BC loop by providing excitation to both the GCs and the BCs. SSR also appears in the population of MCs via interaction with the GCs (i.e., GC-MC loop). Population behaviors in the SSRs are quantitatively characterized in terms of the synchronization measures. In addition, we investigate individual firing activity of GCs, BCs, and MCs in the SSRs. Individual GCs exhibit random spike skipping, leading to a multi-peaked inter-spike-interval histogram, which is well characterized in terms of the random phase-locking degree. In this case, population-averaged mean-firing-rate (MFR) $\langle f_i^{(GC)} \rangle$ is less than the population frequency f_p . On the other hand, both BCs and MCs show “intraStripe” burstings within stripes, together with random spike skipping. Thus, the population-averaged MFR $\langle f_i^{(X)} \rangle$ ($X = \text{MC}$ and BC) is larger than f_p , in contrast to the case of the GCs. MC loss may occur during epileptogenesis. With decreasing the fraction of the MCs, changes in the population and individual firings in the SSRs are also studied. Finally, quantitative association between the population/individual firing behaviors in the SSRs and the winner-take-all competition is discussed.

Keywords Hippocampal dentate gyrus · Sparsely synchronized rhythms · Random spike skipping · IntraStripe bursting

Introduction

The hippocampus, composed of the dentate gyrus (DG) and the areas CA3, CA2, and CA1, plays important roles in memory formation, storage, and retrieval (Gluck and Myers 2001; Squire 1987; Dudek et al. 2016). The DG is

the gateway to the hippocampus, and its primary cells, the so-called granule cells (GCs), receive excitatory inputs from the entorhinal cortex (EC) through the perforant paths (PPs). As a pre-processor for the CA3, the GCs perform pattern separation on the input patterns from the EC by sparsifying and orthogonalizing them (i.e., transforming a set of input patterns into sparser and more distinct patterns), and project the pattern-separated outputs to the pyramidal cells in the CA3 via the mossy fibers (MFs) (Marr 1971; Willshaw and Buckingham 1990; McNaughton and Morris 1987; Rolls 1989a, b, c; Treves and Rolls 1991, 1992, 1994; O’Reilly and McClelland 1994; Schmidt et al. 2012; Rolls 2016; Knierim and Neunuebel 2016; Myers and Scharfman 2009, 2011; Myers et al. 2013; Scharfman and Myers 2016; Yim et al. 2015; Chavlis et al.

✉ Woochang Lim
wclim@icn.re.kr

Sang-Yoon Kim
sykim@icn.re.kr

¹ Institute for Computational Neuroscience and Department of Science Education, Daegu National University of Education, Daegu 42411, Korea

2017; Kassab and Alexandre 2018; Beck et al. 2000; Nitz and McNaughton 2004; Leutgeb et al. 2007; Bakker et al. 2008; Yassa and Stark 2011; Santoro 2013; Dijk and Fenton 2018). The sparse, but relatively strong MFs are known to play a role of “teaching inputs” which tend to trigger synaptic plasticity between the pyramidal cells in the CA3 and also between the pyramidal cells and the EC cells (Treves and Rolls 1994; O’Reilly and McClelland 1994; Schmidt et al. 2012; Rolls 2016; Knierim and Neunuebel 2016; Myers and Scharfman 2009, 2011; Myers et al. 2013; Scharfman and Myers 2016; Kassab and Alexandre 2018). Then, a new pattern may be stored in modified synapses. In this way, pattern separation in the DG facilitates pattern storage and retrieval in the CA3.

In this paper, we pay attention to the DG. The whole GCs in the DG are grouped into the lamellar clusters (Andersen et al. 1971; Amaral and Witter 1989; Andersen et al. 2000; Sloviter and Lømo 2012). In each GC cluster, there is one inhibitory (I) basket cell (BC) along with excitatory (E) GCs, and they form a dynamical E-I loop. During the process of pattern separation, the GCs make sparse firing activity via the winner-take-all competition (Coultrip et al. 1992; Almeida et al. 2009; Petrantonakis and Poirazi 2014, 2015; Houghton 2017; Espinoza et al. 2018; Su et al. 2019; Barranca et al. 2019; Bielczyk et al. 2019; Wang et al. 2020). Only strongly active GCs survive under the feedback inhibition of the BC (i.e., they become winners), while weakly active GCs become silent in response to the feedback inhibition from the BC. The sparsity (resulting from the winner-take-all competition) has been thought to enhance the pattern separation (Treves and Rolls 1994; O’Reilly and McClelland 1994; Schmidt et al. 2012; Rolls 2016; Knierim and Neunuebel 2016; Myers and Scharfman 2009, 2011; Myers et al. 2013; Scharfman and Myers 2016; Chavlis et al. 2017; Kassab and Alexandre 2018).

Here, we are concerned about population rhythms in the DG. For example, gamma rhythms were observed to emerge for communication between the DG and the EC, and between the DG and the CA3 (Fernández-Ruiz et al. 2021; Hsiao et al. 2016), and also observed to appear in the DG, CA3, and CA1 regions during behaving states of rats (Csicsvari et al. 2003). In addition, decrease in the amplitude of theta rhythm and increase in the amplitude of beta rhythm were observed in the DG while performing different associative tasks via presentation of meaningful cues (Rangel et al. 2015). In this paper, we consider sparsely synchronized rhythms (SSRs) which emerge during pattern separation via winner-take-all competition. SSRs are found to appear in each population of the GCs and the BCs via interaction of excitation of the GCs and inhibition of the BCs in the GC-BC loop. In addition to the excitatory GCs, there exist another type of excitatory hilar mossy cells

(MCs). The MCs control the firing activity of the GC-BC loop by providing excitation to both the GCs and the BCs. SSR is also found to appear in the population of MCs via interaction with the GCs (i.e., GC-MC loop). Thus, in the whole DG network, SSRs appear in the populations of the GCs, the MCs, and the BCs, together with occurrence of the winner-take-all competition.

Various SSRs, associated with diverse cognitive functions (e.g., sensory perception, feature integration, selective attention), were observed in the hippocampus, the neocortex, the cerebellum, and the olfactory system (Csicsvari et al. 1999; Destexhe and Paré 1999; Fellous and Sejnowski 2000; Hasenstaub et al. 2005; Solages et al. 2008; Rojas-Líbano and Kay 2008). In these SSRs, at the population level, sparsely synchronous oscillations have been observed in local field potential recordings, while at the cellular level, individual neuronal recordings have been observed to exhibit intermittent and irregular discharges like Geiger counters. Thus, in the SSRs, single-cell firing activity differs markedly from the population oscillatory behaviors, in contrast to the fully synchronized rhythms where individual cells fire regularly at the population frequency like clocks (Wang 2010).

In this paper, we investigate the population behaviors in the SSRs appearing in the DG. Population synchronization may be well visualized in the raster plot of spikes which is a collection of spike trains of individual cells. As a collective quantity showing population behaviors, we use an instantaneous population spike rate (IPSR) which may be obtained from the raster plots of spikes (Wang 2010; Brunel and Wang 2003; Geisler et al. 2005; Brunel and Hakim 2008; Kim and Lim 2018, 2014). For a synchronous case, “stripes” (composed of spikes and indicating population synchronization) are found to be formed in the raster plot, while in a desynchronized case spikes are completely scattered. Hence, in the synchronous case, an oscillating IPSR appears, while for the desynchronized case the IPSR is nearly stationary (Wang 2010; Brunel and Wang 2003; Geisler et al. 2005; Brunel and Hakim 2008; Kim and Lim 2018, 2014). In the case of SSR in the DG, sparsely synchronized stripes appear successively in the raster plot of spikes, and the corresponding IPSR exhibits sparsely synchronized oscillation with the population frequency f_p ($= 13.1$ Hz) [e.g., see the raster plot of spikes for the GCs in Fig. 2a1 and the IPSR in Fig. 2a2]. We note that, in the case of SSR only a fraction of cells make spikings in each stripe in the raster plot of spikes, in contrast to the fully synchronized rhythm where all cells fire spikings in each stripe (Wang 2010). Then, population behaviors in the SSRs in the DG are quantitatively characterized by employing diverse synchronization measures introduced in our prior works. The overall synchronization degree for the

SSR may be well measured in terms of a thermodynamic amplitude measure, given by the time-averaged amplitude of the macroscopic IPSR (Kim and Lim 2021c). In addition, we use the statistical-mechanical spiking measure, given by the product of the occupation degree (representing the spike density in each stripe) and the pacing degree between the spikes (Kim and Lim 2014), and make intensive characterization of the population behaviors in the SSRs.

In addition to the population behaviors, we also study the individual firing behaviors of the GCs, the MCs, and the BCs in the SSRs. Active GCs exhibit intermittent spikings phase-locked to the IPSR at random multiples of the global period T_G of the IPSR. This random phase locking results in random spike skipping, which is well shown in the inter-spike-interval (ISI) histogram with multiple peaks appearing at integer multiples of T_G [e.g., see the ISI histogram of the GCs in Fig. 2c; spiking may occur most probably after 5- and 6-times spike skipping because the middle 6th- and the 7th-order peaks are the highest ones], in contrast to the case of fully synchronized rhythm with only one peak at T_G (i.e., all cells fire regularly at each global cycle without skipping). Similar skipping phenomena of spikings were also observed in the case of fast sparse synchronization occurring in the systems consisting of the two excitatory and inhibitory populations or in the single inhibitory population (Wang 2010; Brunel and Wang 2003; Geisler et al. 2005; Brunel and Hakim 2008; Kim and Lim 2018, 2014). Due to random spike skipping, population-averaged mean-firing-rate (MFR) $\langle f_i^{(\text{GC})} \rangle (= 2.0\text{Hz})$ becomes less than the population frequency $f_p (= 13.1\text{Hz})$. We also introduce a new random phase-locking degree and characterize the random spike skipping. In contrast to the GCs, both MCs and BCs exhibit burstings within stripes, along with random spike skipping. Hence, the ISI histogram becomes composed of the dominant bursting peak and the multiple random-spike-skipping peaks. Due to the dominant bursting peak, the population-averaged MFR $\langle f_i^{(X)} \rangle$ ($X = \text{MC}$ and BC) is larger than f_p , in contrast to the case of the GCs.

Finally, we note that, during epileptogenesis MF sprouting and hilar cell (MC and HIPP cell) death occur (Santhakumar et al. 2005; Morgan et al. 2007). Here, we are concerned about the MC loss. According to the dormant BC hypothesis (Sloviter 1991, 1994), MC loss leads to excitatory denervation of the BCs, resulting in hypoactive inhibition of the GCs, which in turn contributes to hyperexcitability of the GCs. On the other hand, based on the irritable MC hypothesis (Santhakumar et al. 2000; Ratzliff et al. 2002, 2004), surviving MCs with increased excitability amplify hyperexcitability of the GCs. In our work, by decreasing the fraction of the MCs, we investigate

how the population and individual firings in the SSRs change. Quantitative correlation between the population/individual firing behaviors in the SSRs and the winner-take-all competition is also studied.

This paper is organized as follows. In Sect. 2, we describe a spiking neural network of the hippocampal DG. Then, in the main Sect. 3, we investigate population and individual behaviors in the SSRs of the GCs, the MCs, and the BCs. Finally, we give summary and discussion in Sect. 4.

Spiking neural network of the dentate gyrus

In this section, we describe our spiking neural network of the DG. We first developed our DG spiking neural network in the work for the winner-take-all competition (Kim and Lim 2021d), based on the anatomical and the physiological properties given in (Myers and Scharfman 2009; Chavlis et al. 2017). In the present work for the SSR, most of the system parameters for the structure, the single neuron models, and the synaptic currents are the same as those in the work for the winner-take-all competition (Kim and Lim 2021d), except for a few differences (e.g., number of GC clusters). Obviously, our spiking neural network will not capture all the detailed anatomical and physiological complexity of the DG. But, with a limited number of essential elements and synaptic connections in our DG network, population and individual firing behaviors in the SSRs could be successfully studied. Therefore, our spiking neural network model would build a foundation upon which additional complexity may be added and guide further research.

Framework of the spiking neural network of the dentate gyrus

Figure 1 shows the box diagram for our DG network. The granular layer (composed of the excitatory GCs and the inhibitory BCs) and the hilus [consisting of the excitatory MCs and the inhibitory HIPP (hilar perforant path-associated) cells] constitute the DG. Thus, there exist two types of excitatory cells, GCs and MCs, in contrast to the case of the CA3, CA2, and CA1 with only one kind of excitatory pyramidal cells. This DG receives the input from the external EC via the PPs and projects its output to the CA3 via the MFs.

Based on the anatomical data given in (Myers and Scharfman 2009; Chavlis et al. 2017), we chose the numbers of the constituent cells (GCs, BCs, MCs, and HIPP cells) in the DG and the EC cells and the connection probabilities between them. In our work for the winner-take-all competition (Kim and Lim 2021d), we developed a

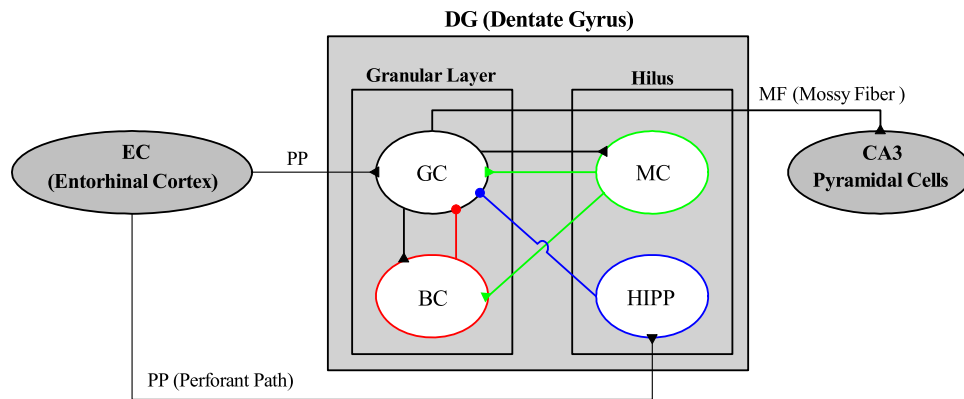


Fig. 1 Box diagram for the hippocampal dentate gyrus (DG) network. Lines with triangles and circles denote excitatory and inhibitory synapses, respectively. In the DG, there are the granular layer [consisting of GC (granule cell) and BC (basket cell)] and the hilus

[composed of MC (mossy cell) and HIPP (hilar perforant path-associated) cell]. The DG receives excitatory input from the EC (entorhinal cortex) via PPs (perforant paths) and provides its output to the CA3 via MFs (mossy fibers)

scaled-down spiking neural network where the total number of excitatory GCs (N_{GC}) was 2,000, corresponding to $\frac{1}{500}$ of the 10^6 GCs found in rats (West et al. 1991). These GCs were grouped into the $N_c (= 20)$ lamellar clusters (Andersen et al. 1971; Amaral and Witter 1989; Andersen et al. 2000; Sloviter and Lømo 2012); in the case of the winner-take-all competition, we chose $N_c (= 100)$ clusters (Kim and Lim 2021d). In each GC cluster, there were $n_{GC}^{(c)} (= 100)$ GCs and one inhibitory BC. Hence, the number of the BCs (N_{BC}) in the whole DG network became 20, corresponding to $1/100$ of N_{GC} (Buckmaster et al. 1996; Buckmaster and Jongen-Rêlo 1999; Buckmaster et al. 2002; Nomura et al. 1997a, b; Morgan et al. 2007). Thus, in each GC cluster, a dynamical GC-BC loop was formed, and the BC (receiving the excitation from all the GCs) provided the feedback inhibition to all the GCs.

The EC layer II is the external source providing the excitatory inputs to the GCs and the HIPP cells via the PPs, as shown in Fig. 1 in Ref. (Myers and Scharfman 2009). The HIPP cells have dendrites extending into the outer molecular layer, where they are targeted by the PPs, along with axons projecting to the outer molecular layer (primarily to the GCs) (Myers and Scharfman 2009; Scharfman 1991; Savanthrapadian et al. 2014; Hosp et al. 2014). Thus, the EC cells and the HIPP cells become the excitatory and the inhibitory input sources to the GCs, respectively. The estimated number of the EC layer II cells (N_{EC}) is about 200,000 in rats, corresponding to 20 EC cells per 100 GCs (Amaral et al. 1990). Thus, we chose $N_{EC} = 400$ in our DG network. Also, the activation degree D_a of the EC cells was chosen as 10% (McNaughton et al. 1991). Thus, we randomly chose 40 active ones among the 400 EC (layer II) cells. Each active EC cell was modeled in terms of the Poisson spike train with frequency of 40 Hz (Hafting et al. 2005). The random-connection probability $p^{(GC,EC)}$

($p^{(HIPP,EC)}$) from the pre-synaptic EC cells to a post-synaptic GC (HIPP cell) was 20 % (Myers and Scharfman 2009; Chavlis et al. 2017). Thus, each GC or HIPP cell was randomly connected with the average number of 80 EC cells.

Next, we consider the hilus, composed of the excitatory MCs and the inhibitory HIPP cells (Scharfman and Myers 2013; Scharfman 2018; Lübke et al. 1998; Amaral et al. 2007; Jinde et al. 2012, 2013; Ratzliff et al. 2004). In rats, the number of MCs (N_{MC}) is known to change from 30,000 to 50,000, corresponding to 3-5 MCs per 100 GCs (West et al. 1991; Buckmaster and Jongen-Rêlo 1999). In our DG network, we chose $N_{MC} = 80$. Also, the estimated number of HIPP cells (N_{HIPP}) in rats is about 12,000 (Buckmaster and Jongen-Rêlo 1999), which corresponds to about 2 HIPP cells per 100 GCs. Hence, we chose $N_{HIPP} = 40$ in our DG network. For simplicity, as in (Myers and Scharfman 2009; Chavlis et al. 2017), the lamellar cluster organization for the hilar cells was not considered.

In our DG network, the whole MCs and the GCs in each GC cluster were mutually connected with the same 20 % random-connection probabilities $p^{(MC,GC)}$ ($GC \rightarrow MC$) and $p^{(GC,MC)}$ ($MC \rightarrow GC$), independently of the GC clusters (Myers and Scharfman 2009; Chavlis et al. 2017). In this way, the GCs and the MCs formed a dynamical E-E loop. All the MCs also provided the excitation to the BC in each GC cluster (Chavlis et al. 2017). Hence, the BC in the GC cluster received excitatory inputs from all the GCs in the same GC cluster and from all the MCs. In this way, the MCs control the firing activity in the GC-BC loop by providing excitation to both the GCs and the BCs.

We also note that each GC in the GC cluster received inhibition from the randomly-connected HIPP cells with the connection probability $p^{(GC,HIPP)} = 20\%$ (Myers and Scharfman 2009; Chavlis et al. 2017). Hence, the firing

activity of the GCs may be determined through competition between the excitatory inputs from the EC cells and from the MCs and the inhibitory inputs from the HIPP cells.

With the above information on the numbers of the relevant cells and the connection probabilities between them, we developed a one-dimensional ring network for the SSR in the DG, as in the case of the winner-take-all competition in the DG (Kim and Lim 2021d). Due to the ring structure, our network has advantage for computational efficiency, and its visual representation may also be easily made. For the schematic diagrams of the ring networks for the EC, the granular layer and the hilus, refer to Fig. 1b1-b3 in (Kim and Lim 2021d), respectively.

Elements and synaptic currents in the DG spiking neural network

As elements of our DG spiking neural network, we chose leaky integrate-and-fire (LIF) neuron models with additional afterhyperpolarization (AHP) currents which determines refractory periods, like our prior study of cerebellar network (Kim and Lim 2021a, b). This LIF neuron model is one of the simplest spiking neuron models (Gerstner and Kistler 2002). Due to its simplicity, it may be easily analyzed and simulated.

Evolutions of dynamical states of individual cells in the X population are governed by the following equations:

$$C_X \frac{dv_i^{(X)}(t)}{dt} = -I_{L,i}^{(X)}(t) - I_{AHP,i}^{(X)}(t) + I_{ext}^{(X)} - I_{syn,i}^{(X)}(t), \quad (1)$$

$$i = 1, \dots, N_X.$$

Here, N_X is the total number of cells in the X population, $X = GC$ and BC in the granular layer and $X = MC$ and $HIPP$ in the hilus. In Eq. (1), C_X (pF) represents the membrane capacitance of the cells in the X population, and the state of the i th cell in the X population at a time t (msec) is characterized by its membrane potential $v_i^{(X)}(t)$ (mV). The time-evolution of $v_i^{(X)}(t)$ is governed by 4 types of currents (pA) into the i th cell in the X population; the leakage current $I_{L,i}^{(X)}(t)$, the AHP current $I_{AHP,i}^{(X)}(t)$, the external constant current $I_{ext}^{(X)}$ (independent of i), and the synaptic current $I_{syn,i}^{(X)}(t)$. Here, a subthreshold case of $I_{ext}^{(X)} = 0$ was considered for all X (Chavlis et al. 2017).

The 1st type of leakage current $I_{L,i}^{(X)}(t)$ for the i th cell in the X population is given by:

$$I_{L,i}^{(X)}(t) = g_L^{(X)}(v_i^{(X)}(t) - V_L^{(X)}). \quad (2)$$

Here, $g_L^{(X)}$ and $V_L^{(X)}$ are conductance (nS) and reversal potential for the leakage current, respectively. The i th cell fires a spike when its membrane potential $v_i^{(X)}$ reaches a

threshold $v_{th}^{(X)}$ at a time $t_{f,i}^{(X)}$. Then, the 2nd type of AHP current $I_{AHP,i}^{(X)}(t)$ follows after spiking (i.e., $t \geq t_{f,i}^{(X)}$), :

$$I_{AHP,i}^{(X)}(t) = g_{AHP}^{(X)}(t)(v_i^{(X)}(t) - V_{AHP}^{(X)}) \text{ for } t \geq t_{f,i}^{(X)}. \quad (3)$$

Here, $V_{AHP}^{(X)}$ is the reversal potential for the AHP current, and the conductance $g_{AHP}^{(X)}(t)$ is given by an exponential-decay function:

$$g_{AHP}^{(X)}(t) = \bar{g}_{AHP}^{(X)} e^{-(t-t_{f,i}^{(X)})/\tau_{AHP}^{(X)}}. \quad (4)$$

Here, $\bar{g}_{AHP}^{(X)}$ and $\tau_{AHP}^{(X)}$ are the maximum conductance and the decay time constant for the AHP current. As $\tau_{AHP}^{(X)}$ is increased, the refractory period becomes longer.

For the parameter values of the capacitance C_X , the leakage current $I_L^{(X)}(t)$, and the AHP current $I_{AHP}^{(X)}(t)$, refer to Table 1 in (Kim and Lim 2021d); these parameter values are based on physiological properties of the GC, BC, MC, and HIPP cell (Chavlis et al. 2017; Lübke et al. 1998).

We next consider the synaptic current $I_{syn,i}^{(X)}(t)$ into the i th cell in the X population, composed of the following 3 types of synaptic currents:

$$I_{syn,i}^{(X)}(t) = I_{AMPA,i}^{(X,Y)}(t) + I_{NMDA,i}^{(X,Y)}(t) + I_{GABA,i}^{(X,Z)}(t). \quad (5)$$

Here, $I_{AMPA,i}^{(X,Y)}(t)$ and $I_{NMDA,i}^{(X,Y)}(t)$ are the excitatory AMPA (α -amino-3-hydroxy-5-methyl-4-isoxazolepropionic acid) receptor-mediated and NMDA (N -methyl- D -aspartate) receptor-mediated currents from the pre-synaptic source Y population to the post-synaptic i th neuron in the target X population, respectively. On the other hand, $I_{GABA,i}^{(X,Z)}(t)$ is the inhibitory GABA_A (γ -aminobutyric acid type A) receptor-mediated current from the pre-synaptic source Z population to the post-synaptic i th neuron in the target X population.

Like the case of the AHP current, the R (= AMPA, NMDA, or GABA) receptor-mediated synaptic current $I_{R,i}^{(T,S)}(t)$ from the pre-synaptic source S population to the i th post-synaptic cell in the target T population is given by:

$$I_{R,i}^{(T,S)}(t) = g_{R,i}^{(T,S)}(t)(v_i^{(T)}(t) - V_R^{(S)}). \quad (6)$$

Here, $g_{R,i}^{(T,S)}(t)$ and $V_R^{(S)}$ are synaptic conductance and synaptic reversal potential (determined by the type of the pre-synaptic source S population), respectively.

In the case of the R (=AMPA and GABA)-mediated synaptic currents, we get the synaptic conductance $g_{R,i}^{(T,S)}(t)$ from:

$$g_{R,i}^{(T,S)}(t) = K_R^{(T,S)} \sum_{j=1}^{N_S} w_{ij}^{(T,S)} s_j^{(T,S)}(t). \quad (7)$$

Table 1 Parameters for the synaptic currents $I_R^{(GC,S)}(t)$ into the GC. The GCs receive the direct excitatory input from the entorhinal cortex (EC) cells, the inhibitory input from the HIPP cells, the excitatory input from the MCs, and the feedback inhibition from the BCs

Target Cells (T)	GC					
	EC cell		HIPP cell	MC		BC
Source Cells (S)	AMPA	NMDA	GABA	AMPA	NMDA	GABA
Receptor (R)						
$K_R^{(T,S)}$	0.89	0.15	0.12	0.05	0.01	25.0
$\tau_{R,r}^{(T,S)}$	0.1	0.33	0.9	0.1	0.33	0.9
$\tau_{R,d}^{(T,S)}$	2.5	50.0	6.8	2.5	50.0	6.8
$\tau_{R,l}^{(T,S)}$	3.0	3.0	1.6	3.0	3.0	0.85
$V_R^{(S)}$	0.0	0.0	-86.0	0.0	0.0	-86.0

Here, $K_R^{(T,S)}$ is the synaptic strength per synapse for the R -mediated synaptic current from the j th pre-synaptic neuron in the source S population to the i th post-synaptic cell in the target T population. The inter-population synaptic connection from the source S population (with N_s cells) to the target T population is given by the connection weight matrix $W^{(T,S)}$ ($= \{w_{ij}^{(T,S)}\}$) where $w_{ij}^{(T,S)} = 1$ if the j th cell in the source S population is pre-synaptic to the i th cell in the target T population; otherwise $w_{ij}^{(T,S)} = 0$. The fraction of open ion channels at time t is also denoted by $s^{(T,S)}(t)$.

In contrast, in the NMDA-receptor case, some of the post-synaptic NMDA channels are blocked by the positive magnesium ion Mg^{2+} (Jahr and Stevens 1990). Hence, the conductance in the case of NMDA receptor is given by (Chavlis et al. 2017):

$$g_{R,i}^{(T,S)}(t) = \tilde{K}_R^{(T,S)} f(v^{(T)}(t)) \sum_{j=1}^{N_s} w_{ij}^{(T,S)} s_j^{(T,S)}(t). \tag{8}$$

Here, $\tilde{K}_R^{(T,S)}$ is the synaptic strength per synapse, and the fraction of NMDA channels that are not blocked by the Mg^{2+} ion is given by a sigmoidal function $f(v^{(T)}(t))$:

$$f(v^{(T)}(t)) = \frac{1}{1 + \eta \cdot [Mg^{2+}]_o \cdot \exp(-\gamma \cdot v^{(T)}(t))}. \tag{9}$$

Here, $v^{(T)}(t)$ is the membrane of the target cell, $[Mg^{2+}]_o$ is the outer Mg^{2+} concentration, η represents the sensitivity of Mg^{2+} unblock, γ denotes the steepness of Mg^{2+} unblock, and the values of parameters vary depending on the target cell (Chavlis et al. 2017). For simplicity, we make an approximation to replace $f(v^{(T)}(t))$ with $\langle f(v^{(T)}(t)) \rangle$ [i.e., time-averaged value of $f(v^{(T)}(t))$ in the range of $v^{(T)}(t)$ of the target cell]. Then, we introduce an effective synaptic strength $K_{NMDA}^{(T,S)}$ ($= \tilde{K}_{NMDA}^{(T,S)} \langle f(v^{(T)}(t)) \rangle$) by absorbing $\langle f(v^{(T)}(t)) \rangle$ into $K_{NMDA}^{(T,S)}$. Thus, with the scaled-down effective synaptic strength $K_{NMDA}^{(T,S)}$ (including

the average blockage effect of the Mg^{2+} ion), the conductance g for the NMDA receptor may also be well approximated in the same form of conductance as other AMPA and GABA receptors in Eq. (7). In this way, we get all the effective synaptic strengths $K_{NMDA}^{(T,S)}$ from the synaptic strengths $\tilde{K}_{NMDA}^{(T,S)}$ in (Chavlis et al. 2017) by taking into consideration the average blockage effect of the Mg^{2+} ion. Consequently, we can use the same form of synaptic conductance of Eq. (7) in all the cases of $R =$ AMPA, NMDA, and GABA, as in other works [e.g., see (Brunel and Wang 2003)].

The post-synaptic ion channels are opened because of binding of neurotransmitters (emitted from the source S population) to receptors in the target T population. The fraction of open ion channels at time t is represented by $s^{(T,S)}(t)$. The time course of $s_j^{(T,S)}(t)$ of the j th cell in the source S population is given by a sum of double exponential functions $E_R^{(T,S)}(t - t_f^{(j)} - \tau_{R,l}^{(T,S)})$:

$$s_j^{(T,S)}(t) = \sum_{f=1}^{F_j^{(s)}} E_R^{(T,S)}(t - t_f^{(j)} - \tau_{R,l}^{(T,S)}). \tag{10}$$

Here, $t_f^{(j)}$ and $F_j^{(s)}$ are the f th spike time and the total number of spikes of the j th cell in the source S population, respectively, and $\tau_{R,l}^{(T,S)}$ is the synaptic latency time constant for R -mediated synaptic current. The exponential-decay function $E_R^{(T,S)}(t)$ (corresponding to contribution of a pre-synaptic spike occurring at $t = 0$ in the absence of synaptic latency) is given by:

$$E_R^{(T,S)}(t) = \frac{1}{\tau_{R,d}^{(T,S)} - \tau_{R,r}^{(T,S)}} \left(e^{-t/\tau_{R,d}^{(T,S)}} - e^{-t/\tau_{R,r}^{(T,S)}} \right) \cdot \Theta(t). \tag{11}$$

Here, $\Theta(t)$ is the Heaviside step function: $\Theta(t) = 1$ for $t \geq 0$ and 0 for $t < 0$, and $\tau_{R,r}^{(T,S)}$ and $\tau_{R,d}^{(T,S)}$ are synaptic rising

and decay time constants of the R -mediated synaptic current, respectively.

In comparison to those in the case of winner-take-all competition (Kim and Lim 2021d), most of the parameter values, associated with the synaptic currents, are the same, except for the changed synaptic strengths, GC \rightarrow MC: $(K_{AMPA}^{(MC,GC)}, K_{NMDA}^{(MC,GC)}) = (1.52, 0.27)$ and MC \rightarrow BC: $(K_{AMPA}^{(BC,MC)}, K_{NMDA}^{(BC,MC)}) = (0.85, 0.05)$. For completeness, we include Tables 1 and 2 which show the parameter values for the synaptic strength per synapse $K_R^{(T,S)}$, the synaptic rising time constant $\tau_{R,r}^{(T,S)}$, synaptic decay time constant $\tau_{R,d}^{(T,S)}$, synaptic latency time constant $\tau_{R,l}^{(T,S)}$, and the synaptic reversal potential $V_R^{(S)}$ for the synaptic currents into the GCs and for the synaptic currents into the HIPP cells, the MCs and the BCs, respectively. These parameter values are also based on the physiological properties of the relevant cells (Chavlis et al. 2017; Kneisler and Dingledine 1995; Geiger et al. 1997; Bartos et al. 2001; Schmidt-Hieber et al. 2007; Larimer and Strowbridge 2008; Schmidt-Hieber and Bischofberger 2010; Krueppel et al. 2011; Chiang et al. 2012).

All of our source codes for computational works were written from scratch in the programming C language. Then, using the GCC compiler we ran the source codes on personal computers with Intel i5-10210U CPUs (1.6 GHz) and 8 GB of RAM. The number of used personal computers vary (from 1 to 70) depending on the type of jobs. For example, consider the case of Fig. 4a1-a3 where raster plots of spikes are shown for 3 different values for the parameter N_{MC} (number of MCs). In each case of $N_{MC} = 60$ and 30, we ran the source codes on 20 independent personal computers simultaneously to get independent samples of raster plots of spikes, and then chose one representative sample of raster plot of spikes (showing well the long-term population behavior). In the case of $N_{MC} = 0$ with the lowest synchronization degree, we needed 30 personal computers to get enough 30 independent samples

of raster plots of spikes for choice of a representative raster plot of spikes. In this way, we used 70 personal computers for Figs. 4a1-a3. We note that numerical integration of the governing Eq. (1) for the time-evolution of states of individual spiking neurons is done by employing the 2nd-order Runge-Kutta method with the time step 0.1 msec. The Runge-Kutta method for numerical integration is well explained in ordinary textbooks for numerical analysis [e.g., refer to (Press et al. 1992)]. We will release our source codes at the public databases such as the ModelDB.

Population and individual firing behaviors in sparsely synchronized rhythms

In our DG network shown in Fig. 1, the main encoding GCs are found to exhibit SSR during their winner-take-all competition (leading to sparse activation of the GCs). Also, the MCs and the BCs show SSRs via interaction with the GCs through the GC-MC loop and the GC-BC loop, respectively. Population and individual behaviors of these SSRs are investigated in terms of diverse measures for population synchronization and random phase-locking degree for characterization of the ISIs. Quantitative correlations between these behaviors and the winner-take-all competition are shown to exist.

Population and individual behaviors in the sparsely synchronized rhythm of the GCs

Figure 1 shows the external input from the EC. As explained in the subsect. 2.1, there are direct excitatory input from the EC cells and indirect disinhibitory EC input, mediated by the HIPP cells (Myers and Scharfman 2009, 2011; Myers et al. 2013; Scharfman and Myers 2016; Chavlis et al. 2017) [e.g., see Fig. 1 in Ref. (Myers and Scharfman 2009)]. Among the 400 EC cells, randomly-chosen 40 active cells make spikings (i.e., activation

Table 2 Parameters for the synaptic currents $I_R^{(T,S)}(t)$ into the HIPP cell, MC, and BC. The HIPP cells receive the excitatory input from the EC cells, the MCs receive the excitatory input from the GCs, and the BCs receive the excitatory inputs from both the GCs and the MCs

Target Cells (T)	HIPP cell		MC		BC			
	Source Cells (S)		GC		GC		MC	
Receptor (R)	AMPA	NMDA	AMPA	NMDA	AMPA	NMDA	AMPA	NMDA
$K_R^{(T,S)}$	12.0	3.04	1.52	0.27	0.38	0.02	0.85	0.05
$\tau_{R,r}^{(T,S)}$	2.0	4.8	0.5	4.0	2.5	10.0	2.5	10.0
$\tau_{R,d}^{(T,S)}$	11.0	110.0	6.2	100.0	3.5	130.0	3.5	130.0
$\tau_{R,l}^{(T,S)}$	3.0	3.0	1.5	1.5	0.8	0.8	3.0	3.0
$V_R^{(S)}$	0.0	0.0	0.0	0.0	0.0	0.0	0.0	0.0

degree $D_a = 10\%$). Each active EC cell is modeled in terms of the Poisson spike train with frequency of 40 Hz. After a break stage ($t = 0 - 300$ msec), Poisson spike train of each active EC cell follows during the stimulus stage ($t = 300 - 30,300$ msec; the stimulus period T_s is $3 \cdot 10^4$ msec).

We note that each HIPP cell is randomly connected to the average number of 80 EC cells with the connection probability $p^{(\text{HIPP,EC})} = 20\%$, among which the average number of active EC cells is 8. Among the 40 HIPP cells, 37 HIPP cells are found to be active, while the remaining 3 HIPP cells (without receiving excitatory input from the active EC cells) are silent; the activation degree of the HIPP cells is 92.5%. Also, the spikings of the active HIPP cells begin from $t \simeq 320$ msec (i.e. about 20 msec delay for the firing of the HIPP cells with respect to the firing onset ($t = 300$ msec) of the active EC cells).

As a pre-processor for the CA3, the GCs in the DG perform the pattern separation, facilitating the pattern storage and retrieval in the CA3. The GCs make sparse firing activity through competitive learning, which has been thought to improve the pattern separation. The activation degree of the GCs was found to be $D_a = 5.2\%$ (i.e., the total number of active GCs is 104). Also, the active GCs begin to make sparse firings from $t \simeq 340$ msec [i.e. about 40 msec delay for the firing of the GCs with respect to the firing onset ($t = 300$ msec) of the active EC cells]. Dynamical origin for winner-take-all competition, leading to the sparse activation of the GCs, has been studied in our prior work (Kim and Lim 2021d). Winner-take-all competition has been found to occur via competition between the firing activity of the GCs and the feedback inhibition of the BC in each GC cluster. In this case, the hilar MCs has also been found to enhance the winner-take-all competition by providing excitation to both the GCs and the BC.

During the winner-take-all competition, SSR is found to appear in the population of the GCs via interaction of excitation of the GCs with inhibition of the BCs. Population firing activity of the active GCs may be well visualized in the raster plot of spikes which is a collection of spike trains of individual active GCs. Figure 2a1 shows the raster plot of spikes for the active GCs; for convenience, only a part from $t = 300$ to 1,300 msec is shown in the raster plot of spikes. We note that sparsely synchronized stripes (composed of sparse spikes and indicating population sparse synchronization) appear successively.

As a population quantity showing collective behaviors, we use an IPSR (instantaneous population spike rate) which may be obtained from the raster plots of spikes (Wang 2010; Brunel and Wang 2003; Geisler et al. 2005; Brunel and Hakim 2008; Kim and Lim 2018, 2014). To get a smooth IPSR, we employ the kernel density estimation

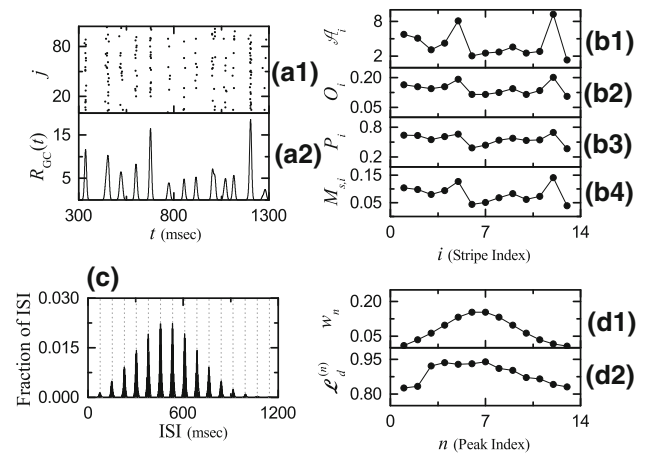


Fig. 2 Emergence of SSR of the GCs. **a1** Raster plot of spikes of 104 active GCs. **a2** IPSR $R_{GC}(t)$ of active GCs. Band width for $R_{GC}(t)$: $h = 20$ msec. Plots of **b1** amplitude \mathcal{A}_i of the IPSR $R_{GC}(t)$, **b2** occupation degree O_i , **b3** pacing degree P_i , and **b4** statistical-mechanical spiking measure $M_{s,i}$ vs. i (spiking stripe index). **c** Population-averaged ISI histogram; bin size = 2 msec. Vertical dotted lines in **c** represent the integer multiples of the global period $T_G^{(\text{GC})}$ ($=76.3$ msec) of $R_{GC}(t)$. Plots of **d1** normalized weight w_n and **d2** random phase-locking degree $\mathcal{L}_d^{(n)}$ for the n th peak of the ISI histogram versus n (random-spike-skipping peak index)

(kernel smoother) (Shimazaki and Shinomoto 2010). Each spike in the raster plot is convoluted (or blurred) with a kernel function $K_h(t)$ to get a smooth estimate of IPSR $R_{GC}(t)$:

$$R_{GC}(t) = \frac{1}{N_a} \sum_{i=1}^{N_a} \sum_{s=1}^{n_i} K_h(t - t_s^{(i)}), \quad (12)$$

where N_a is the number of the active GCs, $t_s^{(i)}$ is the s th spiking time of the i th active GC, n_i is the total number of spikes for the i th active GC, and we use a Gaussian kernel function of band width h :

$$K_h(t) = \frac{1}{\sqrt{2\pi}h} e^{-t^2/2h^2}, \quad -\infty < t < \infty. \quad (13)$$

Throughout the paper, the band width h of $K_h(t)$ is 20 msec. The IPSR $R_{GC}(t)$ of the active GCs is shown in Fig. 2a2, and we note that $R_{GC}(t)$ exhibits synchronous oscillation with the population frequency $f_p^{(\text{GC})}$ ($=13.1$ Hz); in a desynchronized case, the IPSR becomes stationary without oscillation.

In the above way, SSR with the population frequency $f_p^{(\text{GC})}$ ($=13.1$ Hz) [i.e., the global period $T_G^{(\text{GC})}$ (corresponding to the average period between the neighboring spiking stripes) is 76.3 msec] emerges in the population of active GCs. This is similar to the previously-studied case where fast sparse synchronization occurs via E-I balance in the feedback E-I loop (Wang 2010; Brunel and Wang 2003; Geisler et al. 2005; Brunel and Hakim 2008).

We now characterize population firing behavior in the SSR of the GCs by employing the thermodynamic amplitude measure and the statistical-mechanical spiking measure (Kim and Lim 2021c, 2014). The thermodynamic amplitude measure \mathcal{M}_a is given by the time-averaged amplitude of the macroscopic IPSR $R_{GC}(t)$ (Kim and Lim 2021c):

$$\mathcal{M}_a = \overline{\mathcal{A}_i}; \mathcal{A}_i = \frac{R_{GC,max}^{(i)}(t) - R_{GC,min}^{(i)}(t)}{2}, \tag{14}$$

where the overline represents time average, and $R_{GC,max}^{(i)}(t)$ and $R_{GC,min}^{(i)}(t)$ are the maximum and the minimum of $R_{GC}(t)$ in its i th global cycle (corresponding to the i th spiking stripe). As \mathcal{M}_a increases (i.e., the time-averaged amplitude of $R_{GC}(t)$ is increased), the synchronization degree of the SSR becomes higher. Figure 2b1 shows the plot of the amplitude \mathcal{A}_i versus the spiking stripe index i . We follow the 392 stripes during the stimulus period T_s ($= 3 \cdot 10^4$ msec), and thus thermodynamic amplitude measure \mathcal{M}_a (corresponding to the time-averaged amplitude $\overline{\mathcal{A}_i}$) is found to be 3.568.

Next, we characterize the population firing behaviors in terms of the statistical-mechanical spiking measure (Kim and Lim 2014). For a synchronous case, spiking stripes appear successively in the raster plot of spikes. The spiking measure $M_{s,i}$ of the i th stripe is defined by the product of the occupation degree O_i of spikes (denoting the spike density of the i th stripe) and the pacing degree P_i of spikes (representing the degree of phase coherence between spikes in the i th stripe):

$$M_{s,i} = O_i \cdot P_i. \tag{15}$$

The occupation degree O_i of spikes in the i th stripe is given by the fraction of spiking neurons:

$$O_i = \frac{N_i^{(s)}}{N_a}, \tag{16}$$

where $N_i^{(s)}$ is the number of spiking cells in the i th stripe, and N_a is the total number of active cells (e.g., $N_a = 104$ for the GCs). In the case of sparse synchronization, $O_i < 1$, in contrast to the case of full synchronization with $O_i = 1$.

The pacing degree P_i of spikes in the i th stripe can be determined in a statistical-mechanical way by considering their contributions to the macroscopic IPSR $R_{GC}(t)$. Central maxima of $R_{GC}(t)$ between neighboring left and right minima of $R_{GC}(t)$ coincide with centers of spiking stripes in the raster plot. A global cycle begins from a left minimum of $R_{GC}(t)$, passes a maximum, and ends at a right minimum. An instantaneous global phase $\Phi(t)$ of $R_{GC}(t)$ was introduced via linear interpolation in the region forming a global cycle [for details, refer to Eqs. (16) and (17) in (Kim and Lim 2014)]. Then, the contribution of the

k th microscopic spike in the i th stripe occurring at the time $t_k^{(s)}$ to $R_{GC}(t)$ is given by $\cos \Phi_k$, where Φ_k is the global phase at the k th spiking time [i.e., $\Phi_k \equiv \Phi(t_k^{(s)})$]. A microscopic spike makes the most constructive (in-phase) contribution to $R_{GC}(t)$ when the corresponding global phase Φ_k is $2\pi n$ ($n = 0, 1, 2, \dots$). In contrast, it makes the most destructive (anti-phase) contribution to $R_{GC}(t)$ when Φ_k is $2\pi(n - 1/2)$. By averaging the contributions of all microscopic spikes in the i th stripe to $R_{GC}(t)$, we get the pacing degree of spikes in the i th stripe [refer to Eq. (18) in (Kim and Lim 2014)]:

$$P_i = \frac{1}{S_i} \sum_{k=1}^{S_i} \cos \Phi_k, \tag{17}$$

where S_i is the total number of microscopic spikes in the i th stripe. Then, via averaging $M_{s,i}$ of Eq. (15) over a sufficiently large number N_s of stripes (e.g., $N_s = 392$ for the GCs), we obtain the statistical-mechanical spiking measure M_s [refer to Eq. (19) in (Kim and Lim 2014)]:

$$M_s = \frac{1}{N_s} \sum_{i=1}^{N_s} M_{s,i}. \tag{18}$$

Figures 2b2-b4 show the plots of O_i , P_i , and $M_{s,i}$, respectively, in the 13 spiking stripes in Fig. 2a1. By following the 392 stripes during the stimulus period T_s ($= 3 \cdot 10^4$ msec), we get the average occupation $\langle O_i \rangle (= 0.140)$, the average pacing degree $\langle P_i \rangle (= 0.447)$, and the statistical-mechanical spiking measure $M_s (= 0.0626)$. Since $\langle O_i \rangle$ is much less than 1, sparse synchronization occurs. In contrast, moderate pacing ($\langle P_i \rangle = 0.447$) takes place between spikes in each stripe. Thus, the statistical-mechanical spiking measure $M_s (= 0.0626)$, representing the overall synchronization degree, becomes so small, mainly due to low occupation degree.

In addition to the population firing behavior, we also characterize individual spiking behaviors in the SSR. We obtain the ISI histogram for each active GC by collecting the ISIs during the stimulus period T_s ($= 3 \cdot 10^4$ msec), and then get the population-averaged ISI histogram by averaging the individual ISI histograms for all the active GCs. Figure 2c shows the population-averaged ISI histogram. Each active GC exhibits intermittent spikings, phase-locked to $R_{GC}(t)$ at random multiples of its global period $T_G^{(GC)} (= 76.3$ msec). Due to the random spike skipping, distinct 13 multiple peaks appear at the integer multiples of $T_G^{(GC)}$ (denoted by the vertical dotted lines). This is in contrast to the case of full synchronization where only one dominant peak appears at the global period T_G ; all cells fire regularly at each global cycle without skipping. Hereafter, these peaks will be called as the random-spike-skipping

peaks. The middle 6th- and 7th-order peaks are the highest ones, and hence spiking may occur most probably after 5- or 6-times spike skipping. This kind of structure in the ISI histogram is a little different from that in the case of fast sparse synchronization where the highest peak appears at the 1st-order peak, and then the heights of the higher-order peaks decrease successively (Wang 2010; Brunel and Wang 2003; Geisler et al. 2005; Brunel and Hakim 2008; Kim and Lim 2018).

In the case of the active GCs, the average ISI ($\langle \text{ISI} \rangle$) is 498.55 msec. Hence, the population-averaged MFR $\langle f_i^{(\text{GC})} \rangle (= 1/\langle \text{ISI} \rangle)$ is 2.01 Hz, which is much less than the population frequency $f_p^{(\text{GC})} (= 13.1 \text{ Hz})$ of the SSR, in contrast to the case of full synchronization (with full occupation) where the population-averaged MFR is the same as the population frequency.

We introduce a new random phase-locking degree, denoting how well intermittent spikes make phase-locking to $R_{\text{GC}}(t)$ at random multiples of its global period $T_G^{(\text{GC})}$, and characterize the degree of random spike skipping seen in the ISI histogram. By following the approach developed in the case of pacing degree (Kim and Lim 2014), we introduce the random phase-locking degree to examine the regularity of individual firings (represented well in the sharpness of the random-spike-skipping peaks).

We first locate the random-spike-skipping peaks. The range of ISI in the n th-order peak is as follows:

$$(n - \frac{1}{2})T_G^{(\text{GC})} < \text{ISI} < (n + \frac{1}{2})T_G^{(\text{GC})} \text{ for } n \geq 2, \tag{19}$$

$$0 < \text{ISI} < \frac{3}{2}T_G^{(\text{GC})} \text{ for } n = 1. \tag{20}$$

For each n th-order peak, we get the normalized weight w_n , given by:

$$w_n = \frac{N_{\text{ISI}}^{(n)}}{N_{\text{ISI}}^{(\text{tot})}}, \tag{21}$$

where $N_{\text{ISI}}^{(\text{tot})}$ is the total number of ISIs obtained during the stimulus period ($T_s = 3 \cdot 10^4$ msec) and $N_{\text{ISI}}^{(n)}$ is the number of the ISIs in the n th-order peak. For the GCs, $N_{\text{ISI}}^{(\text{tot})} = 6,266$. Figure 2d1 shows the plot of w_n versus n (peak index) for all the 13 peaks. The middle highest 6th and 7th-order peaks have $w_6 = 0.153$ and $w_7 = 0.154$.

We now consider the sequence of the ISIs, $\{\text{ISI}_i^{(n)}, i = 1, \dots, N_{\text{ISI}}^{(n)}\}$, within the n th-order peak, and get the random phase-locking degree $\mathcal{L}_d^{(n)}$ of the n th-order peak. Similar to the case of the pacing degree (Kim and Lim 2014), we provide a phase ψ to each $\text{ISI}_i^{(n)}$ via linear interpolation:

$$\psi(\Delta \text{ISI}_i^{(n)}) = \frac{\pi}{T_G^{(\text{GC})}} \Delta \text{ISI}_i^{(n)} \text{ for } n \geq 2, \tag{22}$$

where $\Delta \text{ISI}_i^{(n)} = \text{ISI}_i^{(n)} - nT_G^{(\text{GC})}$, leading to $-\frac{T_G^{(\text{GC})}}{2} < \Delta \text{ISI}_i^{(n)} < \frac{T_G^{(\text{GC})}}{2}$. However, for $n = 1$, ψ varies depending on whether the ISI lies in the left or the right part of the 1st-order peak:

$$\psi(\Delta \text{ISI}_i^{(1)}) = \begin{cases} \frac{\pi}{2T_G^{(\text{GC})}} \Delta \text{ISI}_i^{(1)} \text{ for } -\frac{T_G^{(\text{GC})}}{2} < \text{ISI}_i^{(1)} < 0, \\ \frac{\pi}{T_G^{(\text{GC})}} \Delta \text{ISI}_i^{(1)} \text{ for } 0 < \text{ISI}_i^{(1)} < \frac{T_G^{(\text{GC})}}{2}. \end{cases} \tag{23}$$

Then, the contribution of the $\text{ISI}_i^{(n)}$ to the locking degree $\mathcal{L}_d^{(n)}$ is given by $\cos(\psi_i^{(n)})$; $\psi_i^{(n)} = \psi(\Delta \text{ISI}_i^{(n)})$. An $\text{ISI}_i^{(n)}$ makes the most constructive contribution to $\mathcal{L}_d^{(n)}$ for $\psi_i^{(n)} = 0$, while it makes no contribution to $\mathcal{L}_d^{(n)}$ for $\psi = \frac{\pi}{2}$ or $-\frac{\pi}{2}$. By averaging the matching contributions of all the ISIs in the n th-order peak, we obtain:

$$\mathcal{L}_d^{(n)} = \frac{1}{N_{\text{ISI}}^{(n)}} \sum_i^{N_{\text{ISI}}^{(n)}} \cos(\psi_i^{(n)}). \tag{24}$$

Finally, we get the (overall) random phase-locking degree \mathcal{L}_d via weighted average of the random phase-locking degrees $\mathcal{L}_d^{(n)}$ of all the peaks:

$$\mathcal{L}_d = \sum_{n=1}^{N_p} w_n \cdot \mathcal{L}_d^{(n)} = \frac{1}{N_{\text{ISI}}^{(\text{tot})}} \sum_{n=1}^{N_p} \sum_{i=1}^{N_{\text{ISI}}^{(n)}} \cos(\psi_i^{(n)}), \tag{25}$$

where N_p is the number of peaks in the ISI histogram. Thus, \mathcal{L}_d corresponds to the average of contributions of all the ISIs in the ISI histogram. Figure 2d2 shows the plot of $\mathcal{L}_d^{(n)}$ versus n (peak index) for the 13 random-spike-skipping peaks. In this case, the random phase-locking degree \mathcal{L}_d , characterizing the sharpness of all the peaks, is 0.911. Hence, the GCs make intermittent spikes which are well phase-locked to $R_{\text{GC}}(t)$ at random multiples of its global period $T_G^{(\text{GC})}$.

Population and individual behaviors in the sparsely synchronized rhythms of the MCs and the BCs

In our DG network, the hilar MCs and the GCs are mutually connected with the 20% random connection probabilities $p^{(\text{MC},\text{GC})}$ (GC \rightarrow MC) and $p^{(\text{GC},\text{MC})}$ (MC \rightarrow GC), which leads to formation of the GC-MC dynamical loop. Then, SSR emerges in the population of

the MCs via interaction with the GCs. Also, each BC receives excitation from all the GCs in the same GC cluster, and it provides feedback inhibition to all the GCs. Thus, the GC-BC dynamical loop is formed, and SSR appears in the population of the BCs through interaction with the GCs.

Here, we investigate the population and individual firing behaviors in the SSRs of the MCs and the BCs. Unlike the case of the GCs, all the MCs ($N_{MC} = 80$) and all the BCs ($N_{BC} = 20$) are active ones (i.e., their activation degrees D_a are 100%). Their raster plots of spikes and the corresponding IPSRs [i.e., $R_{MC}(t)$ and $R_{BC}(t)$] are shown in Fig. 3a1-a2 and e1-e2, respectively. As in the case of the GCs, SSRs with the population frequency $f_p^{(X)} (= 13.1 \text{ Hz}; X = \text{MC and BC})$ appear in the populations of the MCs and the BCs via interaction in the GC-MC-BC loop, respectively.

We note that the population frequencies of the IPSRs $R_X(t)$ ($X = \text{GC, MC, and BC}$) are the same through mutual interaction in the GC-MC-BC loop; for convenience, sometimes we denote the population frequency just as f_p without the superscript. However, phase shifts between the SSRs occur as follows. With respect to the excitatory EC input, starting at $t = 300$ msec, the firings of the GCs begin at a delayed time $t \approx 340$ msec. The GCs provide the excitatory inputs to the MCs which then give the excitatory inputs to the BCs. Thus, time-delay occurs for the firings of the MCs and the BCs with respect to the firings of the GCs. This delayed firing of the MCs (BCs) may be seen clearly in the cross-correlation between the IPSR $R_{MC}(t)$ [$R_{BC}(t)$] and $R_{GC}(t)$;

$$C_{X-GC}(\tau) = \frac{\overline{\Delta R_{GC}(t+\tau)\Delta R_X(t)}}{\sqrt{\overline{\Delta R_{GC}^2(t)}}\sqrt{\overline{\Delta R_X^2(t)}}}; X = \text{MC or BC}, \quad (26)$$

where $\overline{\Delta R_X(t)} = R_X(t) - \overline{R_X(t)}$, and the overline denotes the time average. It is thus found that $C_{MC-GC}(t)$ and $C_{BC-GC}(t)$ have the maxima at $\tau = 10$ and 20 msec, respectively. Consequently, the MCs and the BCs begin to fire at delayed time $t \approx 350$ and 360 msec, respectively.

As in the case of the GCs, we characterize population firing behaviors in the SSRs of the MCs and the BCs. We first employ the thermodynamic amplitude measure \mathcal{M}_a , given by the time-averaged amplitude of the macroscopic IPSRs, $R_{MC}(t)$ and $R_{BC}(t)$ (Kim and Lim 2021c). Figure 3b1 and f1 show the plots of the amplitude \mathcal{A}_i versus i (spiking stripe index) in the case of the MCs and the BCs, respectively. We follow the 392 stripes during the stimulus time $T_s (= 3 \cdot 10^4 \text{ msec})$, and thus the thermodynamic amplitude measures \mathcal{M}_a (corresponding to the time-averaged amplitude $\overline{\mathcal{A}_i}$) for the MCs and the BCs are found to

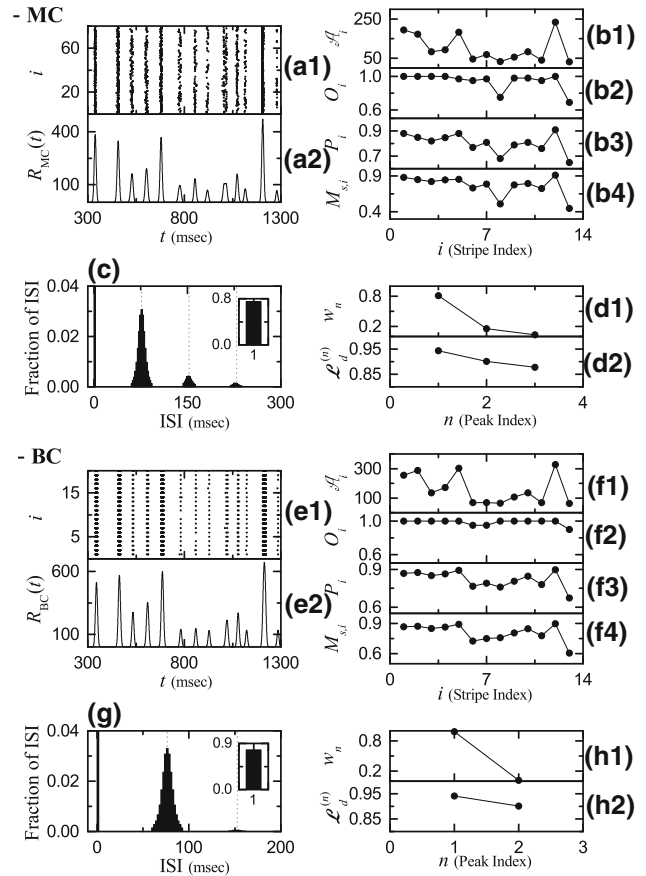


Fig. 3 Emergence of SSR of the MCs. **a1** Raster plot of spikes of MCs. **a2** IPSR $R_{MC}(t)$ of MCs. Plots of **b1** amplitude \mathcal{A}_i of the IPSR $R_{MC}(t)$, **b2** occupation degree O_i , **b3** pacing degree P_i , and **b4** statistical-mechanical spiking measure $\mathcal{M}_{s,i}$ vs. i (spiking stripe index). **c** Population-averaged ISI histogram. Vertical dotted lines in **c** represent the integer multiples of the global period $T_G^{(MC)} (=76.3 \text{ msec})$ of $R_{MC}(t)$. Plots of **d1** normalized weight w_n and **d2** random phase-locking degree $\mathcal{L}_d^{(n)}$ for the n th-order peak of the ISI histogram versus n (random-spike-skipping peak index). Emergence of SSR of the BCs. **e1** Raster plot of spikes of BCs. **e2** IPSR $R_{BC}(t)$ of BCs. Plots of **f1** amplitude \mathcal{A}_i of the IPSR $R_{BC}(t)$, **f2** occupation degree O_i , **f3** pacing degree P_i , and **f4** statistical-mechanical spiking measure $\mathcal{M}_{s,i}$ vs. i (spiking stripe index). **g** Population-averaged ISI histogram. Vertical dotted lines in (g) represent the integer multiples of the global period $T_G^{(BC)} (=76.3 \text{ msec})$ of $R_{BC}(t)$. Plots of **h1** normalized weight w_n and **h2** random phase-locking degree $\mathcal{L}_d^{(n)}$ for the n th-order peak of the ISI histogram versus n (random-spike-skipping peak index)

be 99.05 and 112.73, respectively, which are much larger than $\mathcal{M}_a (= 3.568)$ for the GCs. Hence, the synchronization degrees of the SSRs for the MCs and the BCs are much higher (about 30 times) than that for the GCs.

Next, we use the occupation degree O_i , the pacing degree P_i , and the statistical-mechanical spiking measure $\mathcal{M}_{s,i}$ (Kim and Lim 2014) for characterization of the population firing behaviors in the SSRs of the MCs and the BCs (Kim and Lim 2014). Figure 3b2-b4 and f2-f4 show

the plots of O_i , P_i , and $M_{s,i}$ in the i th spiking stripes for the MCs and the BCs, respectively. We follow the 392 stripes during the stimulus period T_s ($= 3 \cdot 10^4$ msec), and get the average occupation $\langle O_i \rangle$, the average pacing degree $\langle P_i \rangle$, and the statistical-mechanical spiking measure M_s . The average occupation degrees $\langle O_i \rangle$ of the MCs and the BCs are 0.86 and 0.92, respectively, which are much larger (about 6 times) than that ($= 0.14$) of the GCs. However, since $\langle O_i \rangle$ of the MCs and the BCs are still less than 1, MCs and BCs also exhibit sparsely synchronized firings, but these firings are much less sparse than those of the GCs.

Also, the average pacing degrees $\langle P_i \rangle$ of the MCs and the BCs are 0.73 and 0.77, respectively, which are larger than that ($= 0.447$) of the GCs; the pacing between spikings for the MCs and the BCs are better than that for the GCs. Consequently, the statistical-mechanical spiking measure M_s (representing the overall degree of population synchronization) of the MCs and the BCs are 0.63 and 0.71, respectively, which are much larger (at least 10 times) than that ($= 0.0626$) of the GCs. As explained in Subsec. 3.1, M_s for the GCs becomes very small mainly due to low average occupation degree $\langle O_i \rangle$ ($= 0.14$) (resulting from the sparse firings of the GCs).

In addition to the population behaviors, we also characterize individual spiking behaviors in the SSRs of the MCs and BCs in terms of their ISIs. Figure 3c and g show the population-averaged ISI histograms for the MCs and the BCs, respectively; these ISI histograms are obtained in the same way as in the GCs. Unlike the case of the GCs, the MCs and the BCs exhibit “intra-stripe bursting” (corresponding to repeatedly firing bursts of spikes) within the stripes, in addition to the random-spike-skipping spikes; no intra-stripe bursting occurs for the GCs.

Thus, the ISI histograms consist of the dominant “intra-stripe bursting peak” [located near the ISI ($\simeq 1.10$ msec)], arising from the intra-stripe burstings, as well as the random-spike-skipping peaks [located at the integer multiples of the global period $T_G^{(X)}$ ($= 76.3$ msec); $X = \text{MC}$ and BC], resulting from the random-spike-skipping spikes; the fractions of the ISIs at the intra-stripe bursting peaks are 0.75 and 0.78 for the MCs and the BCs, respectively. In this way, the structure of the ISI histograms for the MCs and the BCs is distinctly different from that for the GCs, due to the occurrence of intra-stripe burstings. Consequently, for the MCs (BCs), the average ISI ($\langle \text{ISI} \rangle$) is 23.5 (17.8) msec, and hence the population-averaged MFR $\langle f_i^{(\text{MC})} \rangle$ ($\langle f_i^{(\text{BC})} \rangle$) ($= 1/\langle \text{ISI} \rangle$) is 42.6 (56.2) Hz, which is higher than the population frequency f_p ($= 13.1$ Hz) of the SSRs, in contrast to the case of the GCs with $\langle f_i^{(\text{GC})} \rangle = 2.01$ Hz (much lower than f_p).

As in the case of the GCs, we also characterize the random spike skipping, leading to the random-spike-

skipping peaks in the ISI histograms, in terms of the random phase-locking degree \mathcal{L}_d , representing how well intermittent random-spike-skipping spikes make phase-locking to $R_X(t)$ at random multiples of its global period $T_G^{(X)}$ ($= 76.3$ msec; $X = \text{MC}$ and BC). Unlike the case of the GCs (with the 13 peaks), only the 3 (2) random-spike-skipping peaks appear for the MCs (BCs), due to appearance of the dominant intra-stripe bursting peak. In this case, the normalized weight w_n for the n th-order random-spike-skipping peak is given by:

$$w_n = \frac{N_{\text{ISI}}^{(n,\text{skip})}}{N_{\text{ISI}}^{(\text{tot},\text{skip})}}, \quad (27)$$

where $N_{\text{ISI}}^{(\text{tot},\text{skip})}$ is the total number of random-spike-skipping ISIs and $N_{\text{ISI}}^{(n,\text{skip})}$ is the number of the ISIs in the n th-order random-spike-skipping peak. Figure 3d1 and h1 show the plots of the normalized weights w_n versus n (random-spike-skipping peak index) for the MCs and the BCs, respectively. Unlike the GCs, the 1st-order skipping peak is dominant; $w_1 = 0.811$ and 0.986 for the MCs and the BCs, respectively; the weights of the remaining higher-order skipping peaks are very low.

We now examine the regularity of individual random-spike-skipping (represented well in the sharpness of the random-spike-skipping peaks) in terms of the random phase-locking degree \mathcal{L}_d , introduced in Eq. (25). Figure 3d2 and h2 show the plots of the random phase-locking degree $\mathcal{L}_d^{(n)}$ of the n th-order random-spike-skipping peak versus n (random-spike-skipping peak index) for the MCs and the BCs, respectively. Then, \mathcal{L}_d , corresponding to the average of contributions of all the ISIs in the ISI histogram, is given by the weighted mean of the random phase-locking degrees $\mathcal{L}_d^{(n)}$ of the n th-order random-spike-skipping peak; \mathcal{L}_d is 0.934 and 0.940 for the MCs and the BCs, respectively. Similar to the case of the GC with $\mathcal{L}_d=0.911$, the values of \mathcal{L}_d are also very high, which implies that the intermittent random-spike-skipping spikes for the MCs and the BCs are well phase-locked to $R_X(t)$ at random multiples of its global period $T_G^{(X)}$ ($X = \text{MC}$ and BC).

Effect of the hilar MCs on population and individual behaviors in the sparsely synchronized rhythms

The hilar MCs control the firing activity of the GC-BC loop by providing excitation to both the GCs and the BCs. Through such control, the MCs were found to play an important role of enhancing the winner-take-all competition in each GC cluster (Kim and Lim 2021d). However, MC loss may occur during epileptogenesis (Santhakumar et al. 2005; Morgan et al. 2007; Sloviter 1991, 1994;

Santhakumar et al. 2000; Ratzliff et al. 2002, 2004), which might be a cause of impaired pattern separation leading to memory interference. Through ablation of the MCs, we study their effect on the firing behaviors in the SSRs of the GCs, MCs, and BCs.

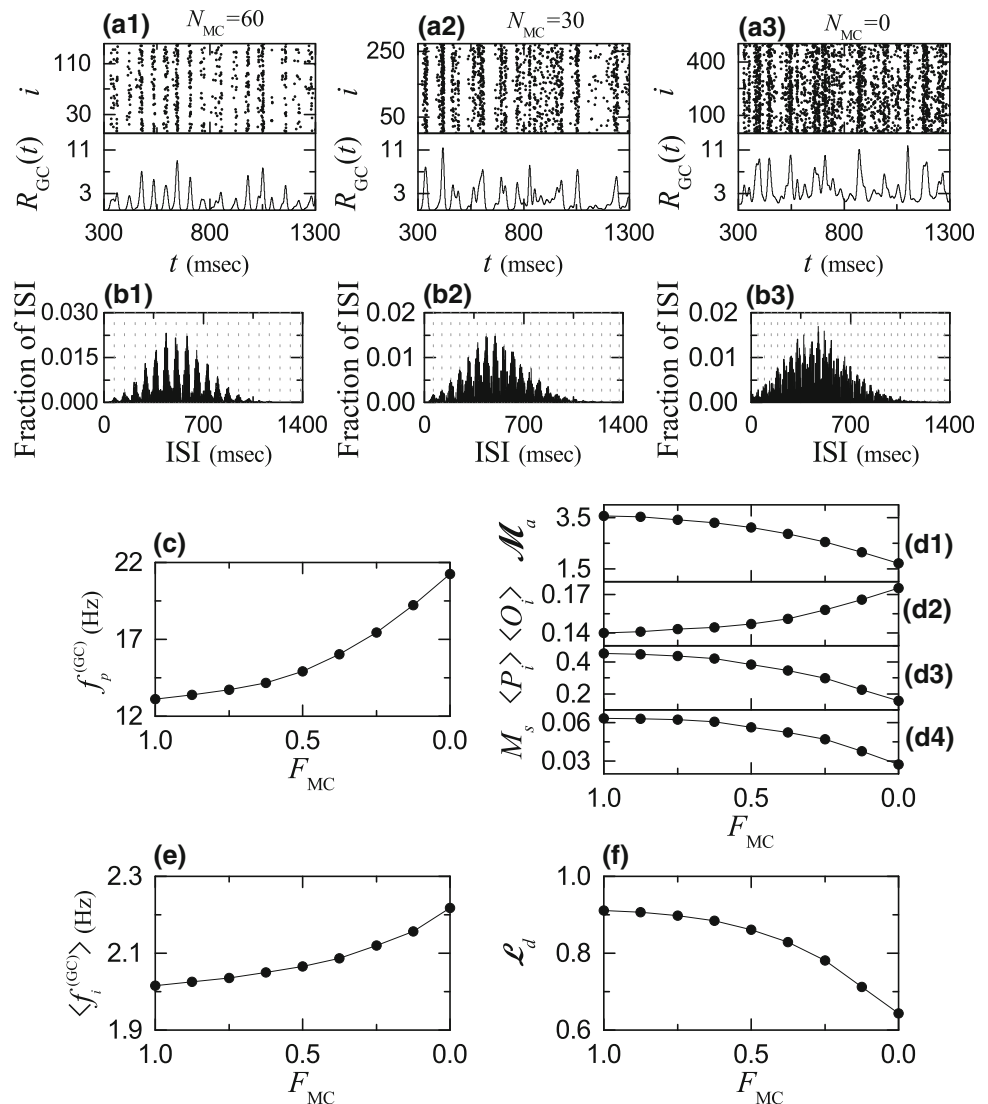
We decrease N_{MC} (number of the MCs) from 80 (in the original whole network) to 0 (complete loss); in this case, the fraction of MCs (F_{MC}) is given by $N_{MC}/80$. With decreasing N_{MC} or equivalently F_{MC} in the above way, we investigate change in the population and individual spiking behaviors in the SSRs of the GCs, the MCs, and the BCs, and compare them with those for $N_{MC} = 80$ (i.e., $F_{MC} = 1$) in Figs. 2 and 3. It is thus found that the MCs play an essential role to enhance the synchronization degree and the random phase-locking degree in the SSRs.

We first consider the case of SSR of the GCs. Figures 4a1-a3 show the raster plots of spikes and the IPSRs $R_{GC}(t)$ for $N_{MC} = 60$ ($F_{MC} = 0.75$), 30 ($F_{MC} = 0.375$),

and 0 ($F_{MC} = 0$), respectively. We note that sparsely synchronized spiking stripes appear successively in the raster plot of spikes and the corresponding IPSR $R_{GC}(t)$ exhibits synchronous oscillations. As N_{MC} is decreased, the interval between the neighboring spiking stripes becomes narrower, and hence the population frequency $f_p^{(GC)}$ of the SSR becomes increased.

With decreasing N_{MC} from 80, the firing activity of the BCs becomes weakened, which leads to decrease in the feedback inhibition to the GCs. Thus, the activation degree D_a of the GCs was found to increase (Sloviter 1991, 1994; Kim and Lim 2021d). Due to such increase in the firing activity of the GCs, spikes in the raster plot become more and more dense, as shown in the case of $N_{MC} = 60, 30$, and 0, which results in increase of the occupation degree O_i (representing the fraction of spiking neurons in each spiking stripe). In contrast, the spiking stripes become more and more smeared, and hence the pacing degree P_i

Fig. 4 Effect of the hilar MCs on the population and individual behaviors in the SSR of the active GCs. Raster plots of spikes and IPSRs $R_{GC}(t)$ for **a1** $N_{MC} = 60$, **a2** $N_{MC} = 30$, and **a3** $N_{MC} = 0$. Population-averaged ISI histograms for **b1** $N_{MC} = 60$, **b2** $N_{MC} = 30$, and **b3** $N_{MC} = 0$. Vertical dotted lines in the ISI histograms represent the integer multiples of the global period $T_G^{(GC)}$ of the SSR; $T_G^{(GC)} = 73.5, 62.9, 47.4$ msec for $N_{MC} = 60, 30$, and 0, respectively. **c** Plot of the population frequency $f_p^{(GC)}$ versus F_{MC} (fraction of MCs). Plots of **d1** the thermodynamic amplitude measure \mathcal{M}_a , **d2** the average occupation degree $\langle O_i \rangle$, **d3** the average pacing degree $\langle P_i \rangle$, and **d4** the statistical-mechanical spiking measure M_s versus F_{MC} . **e** Plot of the population-averaged MFRs $\langle f_i^{(GC)} \rangle$ versus F_{MC} . **f** Plot of the random phase-locking degree \mathcal{L}_d versus F_{MC}



(denoting the degree of phase coherence between spikes) becomes decreased.

Through competition between the occupation and the pacing degrees, the overall synchronization degree of the SSR is determined, which may be well shown in the change in the amplitude \mathcal{A}_i of the IPSR $R_{GC}(t)$; \mathcal{A}_i in the i th global cycle of $R_{GC}(t)$ (i.e., the i th spiking stripe) is given by the difference between the maximum and the minimum of $R_{GC}(t)$ divided by 2 [see Eq. (14)]. With decreasing N_{MC} , the maximum $R_{GC,\max}^{(i)}(t)$ is found to show an increasing tendency, mainly due to the effect of the increased O_i ; the time-averaged maximum $\overline{R_{GC,\max}^{(i)}}(t) = 7.884, 8.112,$ and 8.551 for $N_{MC} = 60, 30,$ and 0 , respectively. However, the minimum $R_{GC,\min}^{(i)}(t)$ exhibits more increasing tendency because of the effects of the increased O_i and the decreased P_i ; the time-averaged minimum $\overline{R_{GC,\min}^{(i)}}(t) = 1.042, 2.376,$ and 5.145 for $N_{MC} = 60, 30,$ and 0 , respectively. Consequently, with decreasing N_{MC} the thermodynamic amplitude measure \mathcal{M}_a (representing the time-averaged amplitude) becomes decreased (i.e., the overall synchronization degree decreases).

By decreasing F_{MC} from 1 to 0, we make more quantitative characterization of the population firing behavior for various values of F_{MC} . Figure 4c and d1-d4 show the plot of the population frequency $f_p^{(GC)}$ versus F_{MC} and the plots of the amplitude measure \mathcal{M}_a , the average occupation degree $\langle O_i \rangle$, the average pacing degree $\langle P_i \rangle$, and the statistical-mechanical spiking measure M_s versus F_{MC} , respectively; all these quantities are obtained by following all the spiking stripes appearing during the stimulus period $T_s (= 3 \cdot 10^4$ msec). As a result of the increased firing activity of the GCs, the population frequency $f_p^{(GC)}$ is found to increase from 13.1 to 21.3 Hz [see Fig. 4c]. The frequency range of the SSR corresponds to the beta rhythm.

The synchronization degree of the SSR with the beta-range $f_p^{(GC)}$ is characterized in terms of the thermodynamic amplitude measure \mathcal{M}_a and the statistical-mechanical spiking measure M_s . As F_{MC} is decreased from 1 to 0, \mathcal{M}_a , [representing the time-averaged amplitude of $R_{GC}(t)$], is found to decrease from 3.568 to 1.703, as shown in Fig. 4d1. Hence, the overall synchronization degree of the SSR becomes decreased. Due to increase in the firing activity of the GCs with decreasing F_{MC} , the average occupation degree $\langle O_i \rangle$ of the spikes becomes increased from 0.14 to 0.175; less sparse spikes appear in the raster plot. In contrast, as F_{MC} is decreased, the average pacing degree $\langle P_i \rangle$ between the spikes is found to decrease from 0.447 to 0.154. Then, the overall synchronization degree of the SSR is determined through competition between the (increasing) occupation and the (decreasing) pacing

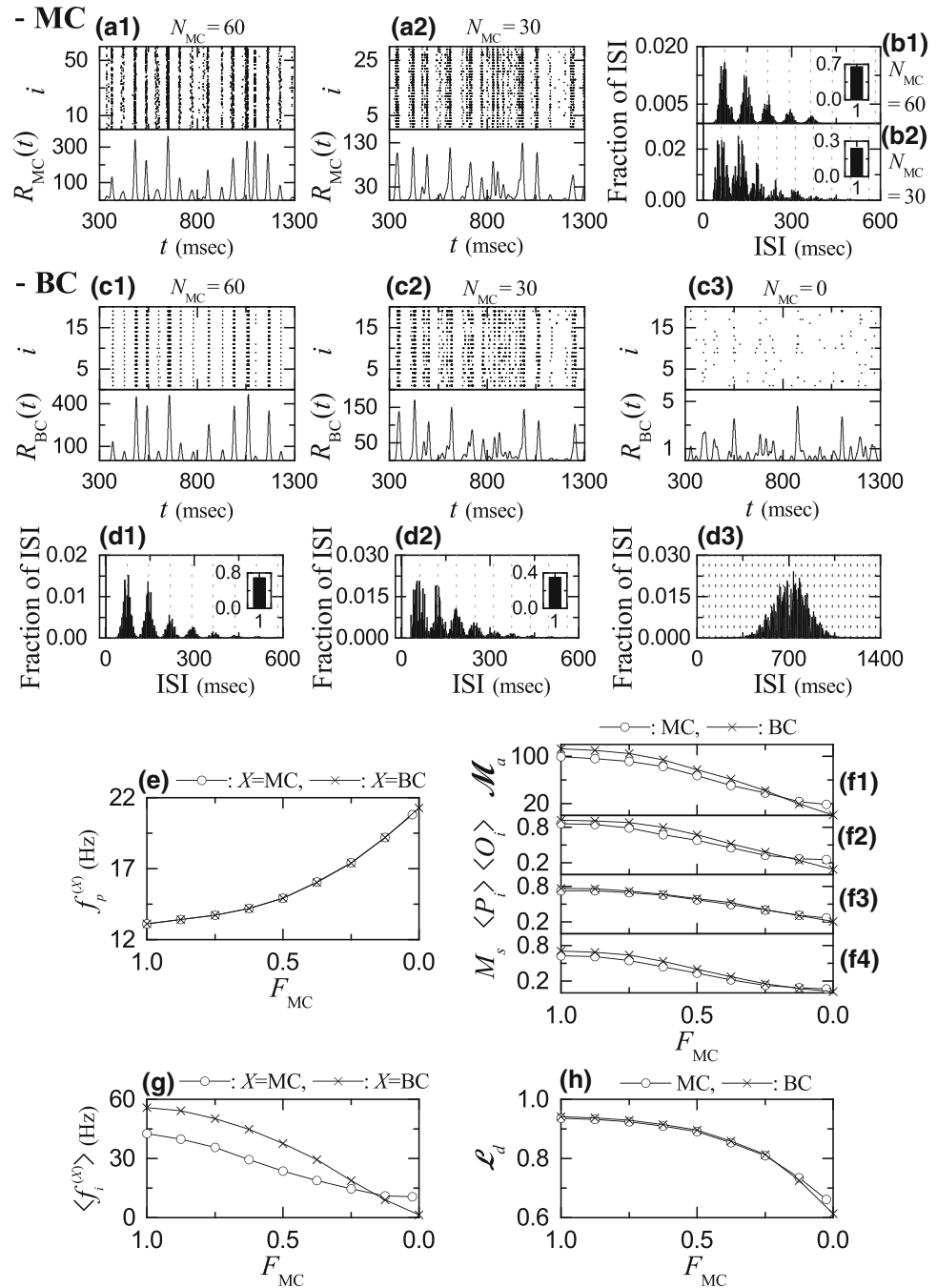
degrees. In this case, the pacing between the spikes becomes much worse, and hence the statistical-mechanical spiking measure M_s , given by the product of the occupation and the pacing degrees, is found to decrease from 0.0626 to 0.027, which is in consistent with the decrease in \mathcal{M}_a .

Next, we consider the individual firing behavior in the SSR of the GCs. Figure 4b1-b3 show the ISI histograms for $N_{MC} = 60, 30,$ and 0 , respectively. The GCs exhibit intermittent random-spike-skipping spikings, locked to $R_{GC}(t)$ at random multiples of the global period $T_G^{(GC)}$ of $R_{GC}(t)$. Due to random spike skipping, the ISI histograms consist of multiple random-spike-skipping peaks. The mean ISIs ($\langle \text{ISI} \rangle$) are 491.1, 479.3, and 451.1 msec, respectively, in the case of $N_{MC} = 60, 30,$ and 0 . Hence, the corresponding population-averaged MFRs $\langle f_i^{(GC)} \rangle (= 1/\langle \text{ISI} \rangle)$ are 2.04, 2.09, and 2.22 Hz, respectively, due to increased activity of the GCs. Moreover, we also note that, as N_{MC} is decreased, the random-spike-skipping peaks become more and more smeared, which results in decrease in the random phase-locking degree \mathcal{L}_d [representing the degree of random phase-locking to $R_{GC}(t)$].

As in the case of the population behavior, with decreasing F_{MC} from 1 to 0, we make more quantitative characterization of the individual firing behavior for various values of F_{MC} . Figures 4e and f show the plots of the population-averaged MFR $\langle f_i^{(GC)} \rangle$ and the random phase-locking degree \mathcal{L}_d , respectively. As F_{MC} is decreased from 1 to 0, $\langle f_i^{(GC)} \rangle$ (given by the reciprocal of the mean ISI) is found to increase from 2.01 to 2.22 Hz, because of the increased firing activity of the GCs. We note that $\langle f_i^{(GC)} \rangle$ is much less than the population frequency $f_p^{(GC)}$, due to random spike skipping. Also, the random phase-locking degree \mathcal{L}_d (characterizing the degree of random spike skipping) is found to exhibit decreasing tendency from 0.911 to 0.641, due to smearing of the random-spike-skipping peaks, as in the decrease in the population synchronization degrees, \mathcal{M}_a and M_s .

From now on, with decreasing N_{MC} , we study the population and individual firing behaviors in the SSRs of the MCs and the BCs. We first consider the cases of $N_{MC} = 60, 30,$ and 0 ; $N_{MC} = 0$ may apply to only the case of the BCs. Figure 5a1-a2 and c1-c3 show the raster plots of spikes and the IPSRs $R_X(t)$ ($X = MC$ and BC) for the MCs and the BCs, respectively. As in the case of the GCs, sparsely synchronized spiking stripes appear successively in the raster plots of spikes and the corresponding IPSRs exhibit synchronous oscillations. As N_{MC} is decreased, the interval between the neighboring spiking stripes becomes narrower, and hence the population frequency $f_p^{(X)}$ of the SSR becomes increased.

Fig. 5 Effect of the hilar MCs on the population and individual behaviors in the SSRs of the MCs and the BCs. Raster plots of spikes of the MCs and IPSR $R_{MC}(t)$ for **a1** $N_{MC} = 60$ and **a2** $N_{MC} = 30$. Population-averaged ISI histograms for the MCs for **b1** $N_{MC} = 60$ and **b2** $N_{MC} = 30$. Vertical dotted lines in the ISI histograms represent the integer multiples of the global period $T_G^{(MC)}$ of $R_{MC}(t)$; $T_G^{(MC)} = 73.5$ and 62.9 msec for $N_{MC} = 60$ and 30 , respectively. Raster plots of spikes of the BCs and IPSR $R_{BC}(t)$ for **c1** $N_{MC} = 60$, **c2** $N_{MC} = 30$, and **c3** $N_{MC} = 0$. Population-averaged ISI histograms for the BCs for **d1** $N_{MC} = 60$, **d2** $N_{MC} = 30$, and **d3** $N_{MC} = 0$. Vertical dotted lines in the ISI histograms represent the integer multiples of the global period $T_G^{(BC)}$ of $R_{BC}(t)$; $T_G^{(BC)} = 73.5$, 62.9 , and 47.4 msec for $N_{MC} = 60$, 30 , and 0 , respectively. **e** Plot of the population frequency $f_p^{(X)}$ versus F_{MC} (fraction of MCs); $X = MC$ (open circle) and BC (cross). Plots of **f1** the thermodynamic amplitude measure \mathcal{M}_a , **f2** the average occupation degree $\langle O_i \rangle$, **f3** the average pacing degree $\langle P_i \rangle$, and **f4** the statistical-mechanical spiking measure M_s versus F_{MC} ; MC (open circle) and BC (cross). **g** Plot of the population-averaged MFRs $\langle f_i^{(X)} \rangle$ versus F_{MC} ; $X = MC$ (open circle) and BC (cross). **h** Plot of the random phase-locking degree \mathcal{L}_d versus F_{MC} ; MC (open circle) and BC (cross)



With decreasing N_{MC} from 80, the firing activities of both the MCs and the BCs become weakened. Hence, unlike the case of the GCs, spikes in the raster plot become more and more sparse, which leads to decrease in the occupation degree O_i (denoting the fraction of spiking neurons in each spiking stripe). Moreover, the spiking stripes become more and more smeared, and hence the pacing degree P_i (representing the degree of phase coherence between spikes) also becomes decreased, as in the case of the GCs.

The overall synchronization degree of the SSRs may be characterized in terms of the thermodynamic amplitude measure \mathcal{M}_a , given by the time-averaged amplitude \overline{A}_i of the IPSR $R_X(t)$; \mathcal{A}_i is given by the difference between the maximum and the minimum of $R_X(t)$ divided by 2. Unlike the case of the GCs, with decreasing N_{MC} , the maximum $R_{GC,max}^{(i)}(t)$ is found to show a decreasing tendency, mainly due to the effect of the decreased O_i . Due to decrease in P_i , $R_{GC,max}^{(i)}(t)$ becomes more decreased. The minimum

$R_{GC,\min}^{(i)}(t)$ is also found to decrease due to decrease in O_i . However, because of decrease in P_i , $R_{GC,\min}^{(i)}(t)$ becomes less decreased. As a result, as N_{MC} is decreased, the amplitude measure \mathcal{M}_a becomes decreased, as in the case of the GCs. Thus, the synchronization degrees of all the SSRs for the GCs, the MCs, and the BCs decrease with decreasing N_{MC} .

Moreover, by decreasing F_{MC} from 1 to 0, we make more quantitative characterization of the population firing behavior for various values of F_{MC} ; for the MCs, instead of $N_{MC} = 0$, we consider the case of $N_{MC} = 2$ (i.e., $F_{MC} = 0.025$) which corresponds to the simplest coupled case. All relevant quantities are obtained by following all the spiking stripes appearing during the stimulus period T_s ($= 3 \cdot 10^4$ msec). Figure 5e shows the plot of the population frequency $f_p^{(X)}$ [$X = MC$ (open circle) and BC (cross)] versus F_{MC} . As F_{MC} is decreased from 1 to 0.025 (MC) and 0 (BC), through interaction with the GCs in the GC-MC and the GC-BC loops, the population frequencies $f_p^{(X)}$ of the SSRs for the MCs and the BCs are found to increase from 13.1 to 20.8 Hz (MC) and 21.3 Hz (BC) in the same way as that for the GCs in Fig. 4c. Thus, the GCs, the MCs, and the BCs exhibit SSRs with the same beta-range population frequency f_p which increases with decreasing F_{MC} .

The synchronization degree of the SSR for the MCs and the BCs may be characterized in terms of the thermodynamic amplitude measure \mathcal{M}_a and the statistical-mechanical spiking measure M_s . Figures 5f1-f4 show the plots of the amplitude measure \mathcal{M}_a , the average occupation degree $\langle O_i \rangle$, the average pacing degree $\langle P_i \rangle$, and the statistical-mechanical spiking measure M_s versus F_{MC} , respectively; MC (open circle) and BC (cross). As F_{MC} is decreased from 1 to 0.025 (MC) and 0 (BC), the thermodynamic amplitude measure \mathcal{M}_a [denoting the time-averaged amplitude of $R_X(t)$ ($X = MC$ and BC)] for the MCs (BCs) is found to decrease rapidly from 99.05 (112.73) to 18.59 (0.98), as in the case of the GCs.

Unlike the case of the GCs, due to decreased firing activity of the MCs (BCs) with decreasing F_{MC} from 1 to 0.025 (0), the average occupation degree $\langle O_i \rangle$ of the spikes becomes decreased from 0.86 (0.92) to 0.26 (0.087); more sparse spikes appear in the raster plot. Similarly, with decreasing F_{MC} , the average pacing degree $\langle P_i \rangle$ between the sparse spikes is also found to decrease from 0.73 (0.77) to 0.27 (0.21) for the MCs (BCs). Then, the statistical-mechanical spiking measure M_s for the MCs (BCs), given by the product of the occupation and the pacing degrees, is found to decrease from 0.63 (0.71) to 0.07 (0.018), which is in consistent with the decrease in \mathcal{M}_a . In this way, as F_{MC} is decreased, the synchronization degrees of the SSRs for the GCs, the MCs, and the BCs become decreased together.

In addition to the population behaviors, we also study the individual firing behaviors in the SSRs of the MCs and the BCs. Figure 5b1-b2 and d1-d3 show the ISI histograms for the MCs and the BCs, respectively. Unlike the GCs, both the MCs and the BCs exhibit intrastripe burstings as well as intermittent random-spike-skipping spikings, locked to the IPSR $R_X(t)$ ($X = MC$ and BC) at random multiples of the global period $T_G^{(X)}$ of $R_X(t)$. As a result, the ISI histograms for the MCs and the BCs consist of both the intrastripe bursting peak and the random-spike-skipping peaks.

We note that, with decreasing N_{MC} , the intrastripe bursting activity of the MCs and the BCs becomes weakened, and hence the height of the intrastripe bursting peak becomes decreased, which results in development of the random-spike-skipping peaks; e.g., more and more higher-order skipping peaks appear, in comparison to the case of $N_{MC} = 80$ in Fig. 3. Particularly, in the case of the BCs, when passing $N_{MC} = 9$ (i.e., $F_{MC} = 0.1125$), intrastripe bursting peak is found to disappear; for the MCs intrastripe bursting peak persists for $N_{MC} = 2$. Thus, only the random-spike-skipping peaks appear for $N_{MC} = 0$ in Fig. 5d3. In this way, with decreasing N_{MC} the random-spike-skipping peaks become more and more developed; particularly, more development occurs for the BCs than the MCs. Hence, the mean ISIs ($\langle ISI \rangle$) become increased for the MCs and the BCs, which results in decrease in the population-averaged MFRs $\langle f_i^{(X)} \rangle$ ($X = MC$ and BC).

Thus, as F_{MC} is decreased from 1 to 0.025 (0) for the MCs (BCs), $\langle f_i^{(X)} \rangle$ ($X = MC$ and BC) is found to decrease from 42.6 (56.2) to 10.6 (1.3) Hz [see Fig. 5g], in contrast to the increase in $\langle f_i^{(GC)} \rangle$ for the GCs in Fig. 4e. Unlike the case of the GCs, for large F_{MC} with strong intrastripe burstings, the population-averaged MFRs $\langle f_i^{(X)} \rangle$ are higher than the population frequency f_p . However, as F_{MC} is decreased, the intrastripe bursting activity becomes decreased, and then the random-spike-skipping activity becomes intensified. Then, for small F_{MC} with strong random-spike-skipping activity (i.e., intrastripe burstings is very weak), $\langle f_i^{(X)} \rangle$ becomes less than f_p , as in the case of the GCs (without intrastripe burstings).

We also note that, as F_{MC} is decreased, the random-spike-skipping peaks become more and more smeared, which leads to decrease in the random phase-locking degree \mathcal{L}_d [denoting the degree of random phase-locking to $R_X(t)$]. With decreasing F_{MC} from 1 to 0.025 (0) for the MCs (BCs), \mathcal{L}_d is found to decrease from 0.934 (0.940) to 0.661 (0.612), as shown in Fig. 5h, as in the case of the GCs. Thus, as F_{MC} is decreased, the random phase-locking degrees for the GCs, the MCs, and the BCs become

decreased together, as in the synchronization degrees of the SSRs.

Finally, we compare the firing behaviors between the MCs and the BCs. For large F_{MC} , the BCs exhibit firing activity with higher MFR $\langle f_i^{(BC)} \rangle$ than the MCs, due to stronger intraburst bursting activity. However, as F_{MC} is sufficiently decreased, the bursting activity of the BCs becomes very weak due to weak excitation from the MCs. Then, $\langle f_i^{(BC)} \rangle$ begins to decrease so rapidly and it becomes lower than $\langle f_i^{(MC)} \rangle$ [see Fig. 5g]. Similarly, for large F_{MC} with strong intrastripe bursting activity, the random phase-locking degree \mathcal{L}_d for the BCs is also a little larger than that for the MCs, while for sufficiently small F_{MC} with so weak intrastripe bursting activity, \mathcal{L}_d for the BCs decreases rapidly and it becomes less than that for the MCs, as shown in Fig. 5h. The population firing behaviors for the MCs and the BCs are also similarly as follows. For large F_{MC} with strong intrastripe bursting activity, \mathcal{M}_a , $\langle O_i \rangle$, $\langle P_i \rangle$, and M_s for the BCs are larger than those for the MCs, while for sufficiently small F_{MC} (with very weak intrastripe bursting activity), those for the MCs become larger than those for the BCs [see Figs. 5f1-f4].

Quantitative relationship between the sparsely synchronized rhythm and the winner-take-all competition

The main encoding GCs was found to exhibit sparse activation via winner-take-all competition in each GC cluster; only strongly active GCs survive under the feedback inhibition of the BC (Kim and Lim 2021d). Such sparsity was thought to improve pattern separation in the DG (Treves and Rolls 1994; O'Reilly and McClelland 1994; Schmidt et al. 2012; Rolls 2016; Knierim and Neunuebel 2016; Myers and Scharfman 2009, 2011; Myers et al. 2013; Scharfman and Myers 2016; Chavlis et al. 2017; Kassab and Alexandre 2018). In Subsec. 3.1, SSR is found to appear in the population of the GCs, along with occurrence of the winner-take-all competition. We investigate the quantitative association between the SSR and the winner-take-all competition.

We first consider association between the measures characterizing the SSR of the GCs. Figure 6a shows the plot of the thermodynamic amplitude measure \mathcal{M}_a versus the statistical-mechanical spiking measure M_s ; plots of \mathcal{M}_a and M_s versus F_{MC} are shown in Fig. 4d1 and d4, respectively. The thermodynamic and statistical-mechanical synchronization degrees, \mathcal{M}_a and M_s , (characterizing the population firing behavior in the SSR) are strongly correlated with the Pearson's correlation coefficient $r = 0.9957$ (Pearson 1895).

Individual firing behaviors of the GCs are characterized in terms of the ISIs. Due to the random spike skipping, the ISI histogram consists of the random-spike-skipping peaks. The random phase-locking degree \mathcal{L}_d is used to characterize the degree of random spike skipping (i.e., degree of sharpness of the random-spike-skipping peaks in the ISI histogram). Figure 6b shows the plot of \mathcal{L}_d versus the average pacing degree $\langle P_i \rangle$; plots of \mathcal{L}_d and $\langle P_i \rangle$ versus F_{MC} are shown in Fig. 4f and d3, respectively. \mathcal{L}_d is found to be strongly correlated with $\langle P_i \rangle$ (characterizing the smearing degree of the spiking stripes in the raster plot of spikes) with the Pearson's correlation coefficient $r = 0.9983$.

We now consider the winner-take-all competition occurring in each GC cluster via competition between the firing activity of the GCs and the feedback inhibition of the BC; for details, refer to (Kim and Lim 2021d). The firing activity of the GCs is determined through competition between the external excitatory (E) to inhibitory (I) inputs to the GCs; two types of E inputs from the EC cells and the MCs and one kind of I input from the HIPP cells. The E-I conductance ratio $\mathcal{R}_{E-I}^{(con)*}$ [given by the time-average of the external E to I conductances in Eq. (22) in (Kim and Lim 2021d)] was found to represent well the degree of the external E-I input competition. GCs with larger $\mathcal{R}_{E-I}^{(con)*}$ than a threshold survived in response to the feedback of the BC (i.e., they became winners). It was thus shown that GCs become active winners when their $\mathcal{R}_{E-I}^{(con)*}$ lies within the winner threshold percentage $W_{th}\%$ of the maximum $\mathcal{R}_{E-I}^{(con)*}(\max)$ of the GC with the strongest activity; see Eq. (23) for $W_{th}\%$ in (Kim and Lim 2021d). As F_{MC} is decreased from 1 to 0, $W_{th}\%$ is found to increase from 15.1% to 55%. Due to the increased $W_{th}\%$, more active GCs appear with decreasing F_{MC} , and hence the winner-take-all competition becomes weaker.

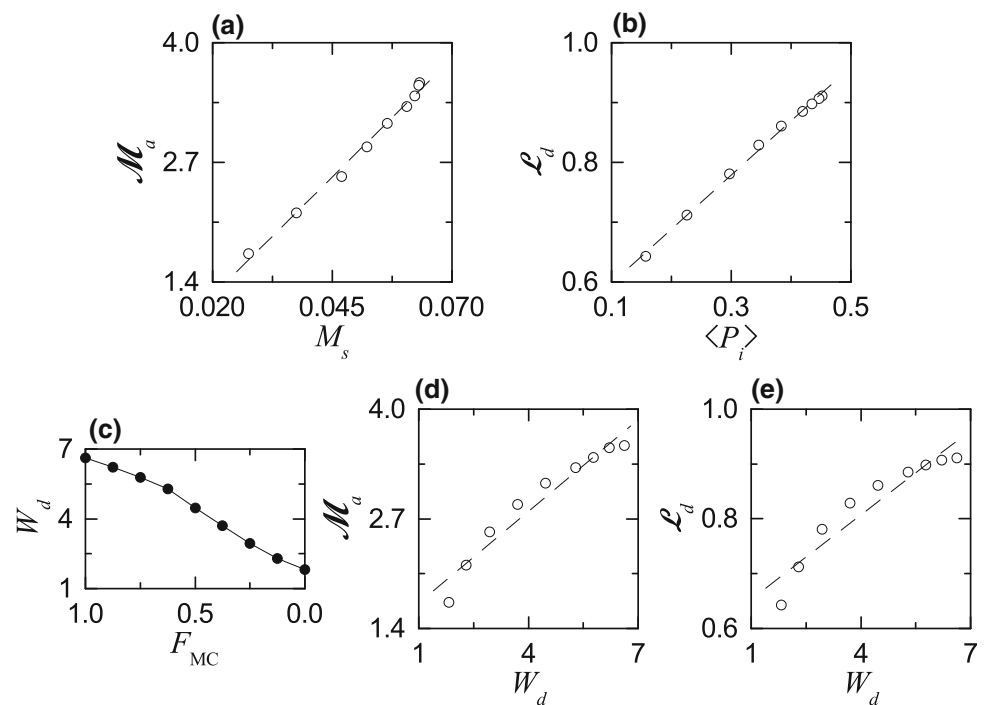
Here, we introduce the winner-take-all competition degree W_d which is reciprocally related to the winner threshold percentage $W_{th}\%$:

$$W_d = \frac{100}{W_{th}\%}. \quad (28)$$

The smaller $W_{th}\%$ is, the larger W_d is. Figure 6c shows the plot of W_d versus F_{MC} . With decreasing F_{MC} , W_d is decreased, and hence the winner-take-all competition becomes weaker.

Figure 6d and 6e show plots of \mathcal{M}_a and \mathcal{L}_d versus W_d , respectively. Population (\mathcal{M}_a) and individual (\mathcal{L}_d) firing behaviors in the SSR are found to be positively correlated with the winner-take-all competition (W_d) with the Pearson's correlation coefficients $r = 0.9705$ and 0.9495 , respectively. Hence, as the winner-take-all competition is

Fig. 6 Quantitative relationship between the SSR and the winner-take-all competition. **a** Plot of the thermodynamic amplitude measure \mathcal{M}_a versus the statistical-mechanical spiking measure M_s . **b** Plot of the random phase-locking degree \mathcal{L}_d versus the average pacing degree $\langle P_i \rangle$. **c** Plot of the winner-take-all competition degree W_d versus F_{MC} (fraction of the MCs). **d** Plot of \mathcal{M}_a versus W_d . **e** Plot of \mathcal{L}_d versus W_d . Fitted dashed lines are given in **a-e**



stronger, the synchronization and the random phase-locking degrees in the SSR of the GCs become higher.

Summary and discussion

We investigated population and individual behaviors in the SSRs in a spiking neural network of the hippocampal DG. Through interaction of excitation of the GCs with inhibition of the BCs, SSRs have been found to appear in each population of the GCs and the BCs, along with occurrence of the winner-take-all competition in each GC cluster, leading to sparse activation of the GCs. Such sparsity has been known to be directly associated with pattern separation, facilitating pattern storage and retrieval in the area CA3.

In each case of the GCs and the BCs, sparsely synchronized stripes have been found to appear successively in the raster plots of spikes, and the corresponding IPSR $R_X(t)$ ($X = GC$ and BC) exhibited oscillatory behavior with the population frequency $f_p (= 13.1 \text{ Hz})$. Such SSR has also been found to appear in the population of the hilar MCs (controlling the firing activity of the GC-BC loop) via interaction with the GCs in the GC-MC loop. Thus, SSRs of the GCs, the MCs, and the BCs emerged in the whole DG network. Various SSRs, related to diverse cognitive functions, were observed in the hippocampus, the neocortex, the cerebellum, and the olfactory system (Csicsvari et al. 1999; Destexhe and Paré 1999; Fellous and

Sejnowski 2000; Hasenstaub et al. 2005; Solages et al. 2008; Rojas-Líbano and Kay 2008).

We have made intensive characterization of the population behaviors in the SSRs of the GCs, the MCs, and the BCs by employing the following diverse synchronization measures introduced in our prior works. As a thermodynamic synchronization degree, we used the amplitude measure \mathcal{M}_a , given by the time-averaged amplitude of the macroscopic IPSR $R_X(t)$ ($X = GC, MC, \text{ and } BC$) (Kim and Lim 2021c), and characterized the overall synchronization degree of the SSRs. The SSR of the GCs was found to have the lowest amplitude measure ($\mathcal{M}_a = 3.568, 99.05, \text{ and } 112.73$ for the GCs, MCs, and BCs, respectively). Next, we also made characterization of the population behaviors in terms of the statistical-mechanical spiking measure M_s (based on the microscopic spikes in the raster plot), given by the product of the occupation degree $\langle O_i \rangle$ and the pacing degree $\langle P_i \rangle$ (Kim and Lim 2014). Among the 3 SSRs, the SSR of the GCs was the most sparse, because its occupation degree $\langle O_i \rangle (= 0.14)$ was so much less than those in the SSRs of the MCs and the BCs; $\langle O_i \rangle = 0.86$ and 0.92 for the MCs and the BCs, respectively. Also, its pacing degree $\langle P_i \rangle$ between the spikes in the raster plot was lower than those for the MCs and the BCs; $\langle P_i \rangle = 0.447, 0.73, \text{ and } 0.77$, respectively. Consequently, the statistical-mechanical spiking measure M_s of the SSR for the main encoding GCs became the lowest ($M_s = 0.063, 0.63, \text{ and } 0.71$ for the GCs, MCs and the BCs, respectively), mainly due to sparse firing of the GCs (resulting from the winner-take-all competition).

In addition to the population behaviors, we have also investigated individual firing activities in the SSRs of the GCs, the MCs, and the BCs. In the case of GCs, active GCs exhibited intermittent spikings, phase-locked to the IPSR $R_{GC}(t)$ at random multiples of its global period $T_G (= 76.3$ msec). Due to the random spike skipping, the ISI histogram has been found to consist of distinct multiple peaks (called the random-spike-skipping peaks) at the integer multiples of T_G , similar to the cases of previously-found “standard” sparse synchronization (Wang 2010; Brunel and Wang 2003; Geisler et al. 2005; Brunel and Hakim 2008; Kim and Lim 2018, 2014). However, unlike the standard sparse synchronization where the 1st-order peak was the highest one, the middle 6th- and 7th-order peaks were the highest ones. In this multi-peaked ISI histogram, the mean ISI ($\langle ISI \rangle$) was 498.55 msec. Then, the population-averaged MFR of the GCs $\langle f_i^{(GC)} \rangle (= 1/\langle ISI \rangle)$ was 2.0 Hz, which was much less than the population frequency $f_p (= 13.1$ Hz), mainly due to random spike skipping.

Unlike the case of GCs, MCs and BCs have been found to exhibit bursting-like multi-spikings within the stripes. Consequently, the ISI histograms for the MCs and the BCs have been found to have the intrastripe bursting peak, in addition to the random-spike-skipping multi-peaks, in contrast to the standard sparse synchronization with only the random-spike-skipping multi-peaks (Wang 2010; Brunel and Wang 2003; Geisler et al. 2005; Brunel and Hakim 2008; Kim and Lim 2018, 2014). Due to the dominance of the intrastripe bursting peak, the mean ISI ($\langle ISI \rangle$) became shorter; $\langle ISI \rangle = 23.5$ and 17.8 msec for the MCs and the BCs, respectively. Then, the population-averaged MFR for the MCs and the BCs were $\langle f_i^{(X)} \rangle (= 1/\langle ISI \rangle)$ ($X = MC$ or $HIPP$) were 42.6 and 56.2 Hz, respectively, which were higher than the population frequency $f_p (= 13.1$ Hz), due to the intrastripe burstings, which was in contrast to the case of the GCs where $\langle f_i^{(GC)} \rangle$ is less than f_p .

We also introduced a new random phase-locking degree \mathcal{L}_d and characterized the “sharpness” of the random-spike-skipping peaks representing how well the intermittent spikes make phase-locking to $R_{GC}(t)$ at random multiples of its global period T_G . The random phase-locking degree \mathcal{L}_d , characterizing the degree of random spike skipping for the GCs, was a little lower than those of the MCs and the BCs; $\mathcal{L}_d = 0.911, 0.934,$ and 0.940 for the GCs, the MCs, and the BCs, respectively. The order in magnitude of \mathcal{L}_d was the same as that in the synchronization degrees, \mathcal{M}_a and \mathcal{M}_s , for the SSRs.

MC loss may occur during epileptogenesis (Santhakumar et al. 2005; Morgan et al. 2007; Sloviter 1991, 1994; Santhakumar et al. 2000; Ratzliff et al. 2002, 2004). With decreasing F_{MC} (fraction of the MCs) from 1 to 0, we investigated the effect of the MCs on the population and

individual firing behaviors in the SSRs of the GCs, the MCs, and the BCs. As F_{MC} was decreased, the interval between the spiking stripes in the raster plot became narrowed, and the spiking stripes became more and more smeared. Hence, the population frequency f_p of the SSRs showed an increasing tendency and their synchronization degrees became decreased. In the ISI histogram for the GCs, the mean ISI ($\langle ISI \rangle$) became shorter, mainly due to weakened inhibition from the BCs, and hence the population averaged MFR $\langle f_i^{(GC)} \rangle$ increased. Moreover, the random-spike-skipping peaks became more and more smeared, leading to decrease in the random phase-locking degree \mathcal{L}_d .

In the case of the MCs and the BCs, with decreasing F_{MC} , the heights of the intrastripe bursting peaks in their ISI histograms became decreased mainly due to decrease in the firing activity of the MCs, which resulted in intensifying the random-spike-skipping peaks (i.e. more and more higher-order random-spike-skipping peaks appeared). Consequently, the mean ISI ($\langle ISI \rangle$) became longer, which led to decrease in the population-averaged MFR $\langle f_i^{(X)} \rangle$ ($X = MC$ or BC), in contrast to the increase in $\langle f_i^{(GC)} \rangle$ for the GCs. Similar to the case of the GCs, the random phase-locking degree \mathcal{L}_d decreased because the random-spike-skipping peaks became more and more smeared.

We note that the SSR of the GCs appeared along with occurrence of the winner-take-all competition in the GC clusters. Hence, we became concerned about the quantitative correlation between the population and individual behaviors in the SSR and the winner-take-all competition for the GCs. It was thus found that both the synchronization degrees, \mathcal{M}_a and \mathcal{M}_s , and the random phase-locking degree \mathcal{L}_d were positively correlated with the winner-take-all competition degree W_d . Therefore, with decreasing F_{MC} (fraction of the MCs), the synchronization degree of the SSR of the GCs becomes lower, together with decrease in the winner-take-all competition degree W_d . Then, the pattern separation (directly proportional to W_d) in the DG becomes worse. As a result of worsened pattern separation, pattern storage and retrieval in the CA3 would be impaired, which might lead to memory interference

For confirmation of appearance of the SSR of the principal GCs and its relationship with the pattern separation via winner-take-all competition [see Fig. 6d], we propose a real experiment via MC ablation for the SSR of the GCs appearing during the pattern separation. By varying F_{MC} (fraction of MCs), the thermodynamic amplitude measure \mathcal{M}_a (representing the synchronization degree of the SSR) may be experimentally measured by obtaining the time-averaged amplitude of the IPSR of the SSR. Also, we note that the winner-take-all competition degree W_d is inversely correlated to the activation degree D_a which can also be

experimentally obtained (Kim and Lim 2021d). In this way, a set of (\mathcal{M}_a, D_a) may be obtained for several values of F_{MC} . Then, the relationship between \mathcal{M}_a of the SSR and $1/D_a$ (correlated with the winner-take-all competition degree) may be confirmed experimentally. In this way, correlation between the SSR of the GCs and the pattern separation via winner-take-all competition may be examined experimentally; the larger the synchronization degree of the SSR is, the better the pattern separation via the winner-take-all competition becomes.

Finally, we discuss limitations of our present work and future works. In the present work, the population and individual behaviors in the SSRs were found to be positively correlated with the winner-take-all competition. However, this kind of correlation does not imply causal relationship. Hence, in future work, it would be interesting to make intensive investigation on their dynamical causation. Also, in the present work, we studied only the case of ablating the MCs for investigation of their role. Another way to manipulate the function of the MCs is to reduce their effect on the GCs by leaving the MCs intact. Hence, in future, it would also be interesting to study the population and the individual behaviors in the SSRs by varying the synaptic strength $K_R^{(BC,MC)}$ ($R = \text{NMDA and AMPA}$) of the synapse between the MC and the BC for change in the disynaptic effect of the MCs on the GCs ($MC \rightarrow BC \rightarrow GC$).

As the MC loss is increased, the activation degree D_a of the GCs is increased [see Fig. 6c; note that the winner-take-all competition degree W_d is inversely correlated to D_a], mainly due to decrease in the disynaptic inhibition from the MCs, mediated by the BCs (Sloviter 1991, 1994). In this case, the brain might try to keep the homeostatic equilibrium between excitation and inhibition (i.e., to keep the activation degree D_a of the GCs) (Roux et al. 2006; Trapp et al. 2018). In the present work, we did not consider such homeostatic equilibrium. In a future work, for examining occurrence of homeostatic equilibrium, it would be interesting to investigate a possibility that the weight for the inhibitory synapses between the BCs and the GCs ($BC \rightarrow GC$) might be adapted to be increased via synaptic plasticity, which could reduce the increased activation degree of the GCs (resulting from the MC loss).

Moreover, in the present work, we took into consideration the disynaptic inhibitory effect of the MCs on the GCs (i.e., disynaptic inhibition to the GCs, mediated by the BC). However, in our present DG network, we did not consider the synaptic connection from the HIPP cells to the BCs, and hence we could not study the disynaptic effect of the HIPP cells on the GCs (i.e., $HIPP \rightarrow BC \rightarrow GC$). The HIPP cells are known to disinhibit the BC (Santhakumar et al. 2005; Morgan et al. 2007), which results in decrease

in the inhibitory effect of the BC on the GCs. Then, the activity of the GCs may increase. In this way, the disynaptic effect of the HIPP cells on the GCs, mediated by the BC, which tends to increase the activity of the GCs, is in contrast to the disynaptic inhibition from the MCs to the GCs (decreasing the firing activity of the GCs). Hence, in future work, it would be meaningful to investigate the disynaptic effect of the HIPP cells on the GC in a modified DG network (including the synaptic connections from the HIPP cells to the BCs).

As in other works in (Myers and Scharfman 2009, 2011; Myers et al. 2013; Scharfman and Myers 2016; Chavlis et al. 2017), we considered the two kinds of projections from the EC via the PPs (perforant paths): $EC \rightarrow GC$ (direct excitatory path to the GCs) and $EC \rightarrow HIPP \rightarrow GC$ (disynaptic feedforward inhibitory path to the GCs, mediated by the HIPP cells). The HIPP cells have both dendrites and axons extending into the molecular layer (i.e., the location where the PP terminates) (Myers and Scharfman 2009; Scharfman 1991; Savanthrapadian et al. 2014). Such HIPP cells with dendrites in the molecular layer were also known to have lower threshold for stimulation of the EC via PPs than the GCs (Scharfman 1991), and hence they are more easily driven by the stimulation of the PPs than the GCs. In this way, the EC may control the activity of the GCs via balance between the direct excitation and the disynaptic feedforward inhibition (mediated by the HIPP cells). These direct excitatory and the indirect feedforward inhibitory projections from the EC may be a minimal choice necessary for controlling the activity of the GCs. There is another disynaptic feedforward inhibitory path, mediated by the BCs: $EC \rightarrow BC \rightarrow GC$ (Ewell and Jones 2010; Kneisler and Dingledine 1995). In (Yim et al. 2015; Santhakumar et al. 2005; Morgan et al. 2007), the authors considered the disynaptic feedforward inhibition, mediated by the BCs; but, they did not consider the disynaptic feedforward inhibition, mediated by the HIPP cells. We expect that the disynaptic feedforward inhibition effect, mediated by the BCs, would be essentially similar to that, mediated by the HIPP cells in the present study. In a future work, it would be interesting to include another disynaptic feedforward path, mediated by the BCs and compare its effect on the SSR and the pattern separation via the winner-take-all competition with that in the disynaptic feedforward inhibition effect, mediated by the HIPP cells in the present work. Also, study on the combined effect (including both $EC \rightarrow HIPP$ and $EC \rightarrow BC$) would also be interesting in the future work.

Like other previous works in (Myers and Scharfman 2009; Chavlis et al. 2017), we considered a neural network for the DG, receiving the inputs from the EC. In addition to the work in the DG (Myers and Scharfman 2009), the authors extended their DG model to incorporate the CA3

area, which resulted in a combined DG-CA3 network with backprojection from the pyramidal cells in the CA3 to the DG, for investigation of the effect of backprojection on the pattern separation and completion (Myers and Scharfman 2011). Because of the inhibitory backprojection, the activation degree D_a of the GCs was found to be decreased, which led to enhance pattern separation. Hence, as a future work, it would be interesting to study the SSR in a combined DG-CA3 network with backprojection, along with study of pattern separation and completion. Due to inhibition of the backprojection, it is expected that the activation degree D_a of the GCs would be decreased, which would result in increase in the synchronization degree of the SSR in the DG, together with increase in the pattern separation degree via winner-take-all competition. This expectation could be examined in the future work.

Also, in the present study, for simplicity, we did not consider the lamellar organization for the hilar MCs and the HIPP cells, as in (Myers and Scharfman 2009; Chavlis et al. 2017). For more refined DG network, in future work, it would be necessary to take into consideration the lamellar organization for the MCs and the HIPP cells; particularly, in the combined DG-CA3 network, as in (Myers and Scharfman 2011; Myers et al. 2013; Scharfman and Myers 2016).

Funding Information This research was supported by the Basic Science Research Program through the National Research Foundation of Korea (NRF) funded by the Ministry of Education (Grant No. 20162007688).

References

- Almeida LD, Idiart M, Lisman JE (2009) A second function of gamma frequency oscillations: An E%-max winner-take-all mechanism selects which cells fire. *J Neurosci* 29:7497–7503
- Amaral DG, Witter MP (1989) The three-dimensional organization of the hippocampal formation: a review of anatomical data. *Neuroscience* 31:571–591
- Amaral DG, Ishizuka N, Claiborne B (1990) Neurons, numbers and the hippocampal network. *Prog Brain Res* 83:1–11
- Amaral DG, Scharfman HE, Lavenex P (2007) The dentate gyrus: fundamental neuroanatomical organization (dentate gyrus for dummies). *Prog Brain Res* 163:3–22
- Andersen P, Bliss TVP, Skrede KK (1971) Lamellar organization of hippocampal excitatory pathways. *Exp Brain Res* 13:222–238
- Andersen P, Soleng AF, Raastad M (2000) The hippocampal lamella hypothesis revisited. *Brain Res* 886:165–171
- Bakker A, Kirwan CB, Miller M, Stark CEL (2008) Pattern separation in the human hippocampal CA3 and dentate gyrus. *Science* 319:1640–1642
- Barranca VJ, Huang H, Kawakita G (2019) Network structure and input integration in competing firing rate models for decision-making. *J Comput Neurosci* 46:145–168
- Bartos M, Vida I, Frotscher M, Geiger JR, Jonas P (2001) Rapid signaling at inhibitory synapses in a dentate gyrus interneuron network. *J Neurosci* 21:2687–2698
- Beck H, Goussakov IV, Lie A, Helmstaedter C, Elger CE (2000) Synaptic plasticity in the human dentate gyrus. *J Neurosci* 20:7080–7086
- Bielczyk NZ, Piskala K, Płomecka M, Radziński P, Todorova L, Foryś U, (2019) Time-delay model of perceptual decision making in cortical networks. *PLoS One* 14:e0211885
- Brunel N, Hakim V (2008) Sparsely synchronized neuronal oscillations. *Chaos* 18:015113
- Brunel N, Wang XJ (2003) What determines the frequency of fast network oscillations with irregular neural discharges? I. Synaptic dynamics and excitation-inhibition balance. *J Neurophysiol* 90:415–430
- Buckmaster PS, Jongen-Rêlo AL (1999) Highly specific neuron loss preserves lateral inhibitory circuits in the dentate gyrus of kainite-induced epileptic rats. *J Neurosci* 19:9519–9529
- Buckmaster PS, Wenzel HJ, Kunkel DD, Schwartzkroin PA (1996) Axon arbors and synaptic connections of hippocampal mossy cells in the rat in vivo. *J Comp Neurol* 366:271–292
- Buckmaster PS, Yamawaki R, Zhang GF (2002) Axon arbors and synaptic connections of a vulnerable population of interneurons in the dentate gyrus in vivo. *J Comp Neurol* 445:360–373
- Chavlis S, Petrantonakis PC, Poirazi P (2017) Dendrites of dentate gyrus granule cells contribute to pattern separation by controlling sparsity. *Hippocampus* 27:89–110
- Chiang PH, Wu PY, Kuo TW, Liu YC, Chan CF, Chien TC, Cheng JK, Huang YY, Chiu CD, Lien CC (2012) GABA is depolarizing in hippocampal dentate granule cells of the adolescent and adult rats. *J Neurosci* 32:62–67
- Coultrip R, Granger R, Lynch G (1992) A cortical model of winner-take-all competition via lateral inhibition. *Neural Netw* 5:47–54
- Csicsvari J, Hirase H, Czurko A, Mamiya A, Buzsáki G (1999) Oscillatory coupling of hippocampal pyramidal cells and interneurons in the behaving rat. *J Neurosci* 19:274–287
- Csicsvari J, Jamieson B, Wise K, Buzsáki G (2003) Mechanisms of gamma oscillations in the hippocampus of the behaving rat. *Neuron* 37:311–322
- Destexhe A, Paré D (1999) Impact of network activity on the integrative properties of neocortical pyramidal neurons in vivo. *J Neurophysiol* 81:1531–1547
- Dijk van MT, Fenton AA (2018) On how the dentate gyrus contributes to memory discrimination. *Neuron* 98:832–845
- Dudek SM, Alexander GM, Farris S (2016) Rediscovering area CA2: unique properties and functions. *Nat Rev Neurosci* 17:89–102
- Espinoza C, Guzman SJ, Zhang X, Jonas P (2018) Parvalbumin+ interneurons obey unique connectivity rules and establish a powerful lateral inhibition microcircuit in dentate gyrus. *Nat Commun* 9:4605
- Ewell LA, Jones MV (2010) Frequency-tuned distribution of inhibition in the dentate gyrus. *J Neurosci* 30:12597–12607
- Fellous J, Sejnowski TJ (2000) Cholinergic induction of oscillations in the hippocampal slice in the slow (0.5–2 Hz), theta (5–12 Hz) and gamma (35–70 Hz) bands. *Hippocampus* 10:187–197
- Fernández-Ruiz A, Oliva A, Soula M, Rocha-Almeida F, Nagy GA, Martín-Vázquez G, Buzsáki G (2021) Gamma rhythm communication between entorhinal cortex and dentate gyrus neuronal assemblies. *Science* 372:eabf3119
- Geiger JRP, Lübke J, Roth A, Frotscher M, Jonas P (1997) Submillisecond AMPA receptor-mediated signaling at a principal neuron-interneuron synapse. *Neuron* 18:1009–1023
- Geisler C, Brunel N, Wang XJ (2005) Contributions of intrinsic membrane dynamics to fast network oscillations with irregular neuronal discharges. *J Neurophysiol* 94:4344–4361
- Gerstner W, Kistler W (2002) *Spiking Neuron Models*. Cambridge University Press, New York

- Gluck MA, Myers CE (2001) Gateway to memory: an introduction to neural network modeling of the hippocampus in learning and memory. MIT Press, Cambridge
- Hafting T, Fyhn M, Molden S, Moser MB, Moser EI (2005) Microstructure of a spatial map in the entorhinal cortex. *Nature* 436:801–806
- Hasenstaub A, Shu Y, Haider B, Kraushaar U, Duque A, McCormick D (2005) Inhibitory postsynaptic potentials carry synchronized frequency information in active cortical networks. *Neuron* 47:423–435
- Hosp JA, Strüber M, Yanagawa Y, Obata K, Vida I, Jonas P, Bartos M (2014) Morpho-physiological criteria divide dentate gyrus interneurons into classes. *Hippocampus* 24:189–203
- Houghton C (2017) Dentate gyrus and hilar region revisited. *Behav Brain Sci* 39:28–29
- Hsiao YT, Zheng C, Colgin LL (2016) Slow gamma rhythms in CA3 are entrained by slow gamma activity in the dentate gyrus. *J Neurophysiol* 116:2594–2603
- Jahr CE, Stevens CF (1990) Voltage dependence of NMDA-activated macroscopic conductances predicted by single-channel kinetics. *J Neurosci* 10:3178–3182
- Jinde S, Zsiros V, Jiang Z, Nakao K, Pickel J, Kohno K, Belforte JE, Nakazawa K (2012) Hilar mossy cell degeneration causes transient dentate granule cell hyperexcitability and impaired pattern separation. *Neuron* 76:1189–1200
- Jinde S, Zsiros V, Nakazawa K (2013) Hilar mossy cell circuitry controlling dentate granule cell excitability. *Front Neural Circuit* 7:14
- Kassab R, Alexandre F (2018) Pattern separation in the hippocampus: distinct circuits under different conditions. *Brain Struct Funct* 223:2785–2808
- Kim SY, Lim W (2014) Realistic thermodynamic and statistical-mechanical measures for neural synchronization. *J Neurosci Meth* 226:161–170
- Kim SY, Lim W (2018) Effect of inhibitory spike-timing-dependent plasticity on fast sparsely synchronized rhythms in a small-world neuronal network. *Neural Netw* 106:50–66
- Kim SY, Lim W (2021) Effect of diverse recoding of granule cells on optokinetic response in a cerebellar ring network with synaptic plasticity. *Neural Netw* 134:173–204
- Kim SY, Lim W (2021) Influence of various temporal recoding on Pavlovian eyeblink conditioning in the cerebellum. *Cogn Neurodyn*. <https://doi.org/10.1007/s11571-021-09673-2>
- Kim SY, Lim W (2021) Equalization effect in interpopulation spike-timing-dependent plasticity in two inhibitory and excitatory populations. In: Lintas A, Enrico P, Pan X, Wang R, Villa A (eds) *Advances in cognitive neurodynamics (VII)*. Springer, Singapore, p 8
- Kim SY, Lim W (2021d) Dynamical origin for winner-take-all competition in a biological network of the hippocampal dentate gyrus. *bioRxiv*, <https://doi.org/10.1101/2021.5.12.443925>
- Kneisler TB, Dingledine R (1995) Spontaneous and synaptic input from granule cells and the perforant path to dentate basket cells in the rat hippocampus. *Hippocampus* 5:151–164
- Knierim JJ, Neunuebel JP (2016) Tracking the flow of hippocampal computation: Pattern separation, pattern completion, and attractor dynamics. *Neurobiol Learn Mem* 129:38–49
- Krueppel R, Remy S, Beck H (2011) Dendritic integration in hippocampal dentate granule cells. *Neuron* 71:512–528
- Larimer P, Strowbridge BW (2008) Nonrandom local circuits in the dentate gyrus. *J Neurosci* 28:12212–12223
- Leutgeb JK, Leutgeb S, Moser MB, Moser EI (2007) Pattern separation in the dentate gyrus and CA3 of the hippocampus. *Science* 315:961–966
- Lübke J, Frotscher M, Spruston N (1998) Specialized electrophysiological properties of anatomically identified neurons in the hilar region of the rat fascia dentata. *J Neurophysiol* 79:1518–1534
- Marr D (1971) Simple memory: a theory for archicortex. *Phil Trans R Soc Lond B* 262:23–81
- McNaughton B, Morris R (1987) Hippocampal synaptic enhancement and information storage within a distributed memory system. *Trends Neurosci* 10:408–415
- McNaughton BL, Barnes CA, Mizumori SJY, Green EJ, Sharp PE (1991) Contribution of granule cells to spatial representations in hippocampal circuits: A puzzle. In: Morrell F (ed) *Kindling and synaptic plasticity: the legacy of Graham Goddar*. Springer-Verlag, Boston, pp 110–123
- Morgan RJ, Santhakumar V, Soletz I (2007) Modeling the dentate gyrus. *Prog Brain Res* 163:639–658
- Myers CE, Scharfman HE (2009) A role for hilar cells in pattern separation in the dentate gyrus: A computational approach. *Hippocampus* 19:321–337
- Myers CE, Scharfman HE (2011) Pattern separation in the dentate gyrus: A role for the CA3 backprojection. *Hippocampus* 21:1190–1215
- Myers CE, Bermudez-Hernandez K, Scharfman HE (2013) The influence of ectopic migration of granule cells into the hilus on dentate gyrus-CA3 function. *PLoS ONE* 8:e68208
- Nitz D, McNaughton B (2004) Differential modulation of CA1 and dentate gyrus interneurons during exploration of novel environments. *J Neurophysiol* 91:863–872
- Nomura T, Fukuda T, Aika Y, Heizmann CW, Emson PC, Kobayashi T, Kosaka T (1997) Distribution of nonprincipal neurons in the rat hippocampus, with special reference to their dorsoventral difference. *Brain Res* 751:64–80
- Nomura T, Fukuda T, Aika Y, Heizmann CW, Emson PC, Kobayashi T, Kosaka T (1997) Laminar distribution of non-principal neurons in the rat hippocampus, with special reference to their compositional difference among layers. *Brain Res* 764:197–204
- O'Reilly RC, McClelland JC (1994) Hippocampal conjunctive encoding, storage, and recall: Avoiding a tradeoff. *Hippocampus* 4:661–682
- Pearson K (1895) Notes on regression and inheritance in the case of two parents. *Proc R Soc Lond* 58:240–242
- Petrantonakis PC, Poirazi P (2014) A compressed sensing perspective of hippocampal function. *Front Syst Neurosci* 8:141
- Petrantonakis PC, Poirazi P (2015) Dentate gyrus circuitry features improve performance of sparse approximation algorithms. *PLoS One* 10:e0117023
- Press WH, teukolsky SA, Vetterling WT, Flannery BP, (1992) *Numerical recipes in C: the art of scientific computing*, 2nd edn. Cambridge University Press, New York
- Rangel LM, Chiba AA, Quinn LK (2015) Theta and beta oscillatory dynamics in the dentate gyrus reveal a shift in network processing state during cue encounters. *Front Syst Neurosci* 9:96
- Ratzliff AH, Santhakumar V, Howard A, Soltesz I (2002) Mossy cells in epilepsy: rigor mortis or vigor mortis? *Trends Neurosci* 25:140–144
- Ratzliff ADH, Howard AL, Santhakumar V, Osapay I, Soltesz I (2004) Rapid deletion of mossy cells does not result in a hyperexcitable dentate gyrus: Implications for epileptogenesis. *J Neurosci* 24:2259–2269
- Rojas-Libano D, Kay LM (2008) Olfactory system gamma oscillations: the physiological dissection of a cognitive neural system. *Cogn Neurodyn* 2:179–194
- Rolls ET (1989) Functions of neuronal networks in the hippocampus and neocortex in memory. In: Byrne JH, Berry WO (eds) *Neural models of plasticity: experimental and theoretical approaches*. Academic Press, San Diego, pp 240–265

- Rolls ET (1989) The representation and storage of information in neural networks in the primate cerebral cortex and hippocampus. In: Durbin R, Miall C, Mitchison G (eds) *Comput Neuron*. Addison-Wesley, Wokingham, pp 125–159
- Rolls ET (1989) Functions of neuronal networks in the hippocampus and cerebral cortex in memory. In: Cotterill R (ed) *Models Brain Function*. Cambridge University Press, New York, pp 15–33
- Rolls ET (2016) Pattern separation, completion, and categorization in the hippocampus and neocortex. *Neurobiol Learn Mem* 129:4–28
- Roux NL, Amar M, Baux G, Fossier P (2006) Homeostatic control of the excitation-inhibition balance in cortical layer 5 pyramidal neurons. *Eur J Neurosci* 24:3507–3518
- Santhakumar V, Bender R, Frotscher M, Ross ST, Hollrigel GS, Toth Z, Soltesz I (2000) Granule cell hyperexcitability in the early post-traumatic rat dentate gyrus: the “irritable mossy cell” hypothesis. *J Physiol* 524:117–134
- Santhakumar V, Aradi I, Soltesz I (2005) Role of mossy fiber sprouting and mossy cell loss in hyperexcitability: A network model of the dentate gyrus incorporating cell types and axonal topography. *J Neurophysiol* 93:437–453
- Santoro A (2013) Reassessing pattern separation in the dentate gyrus. *Front Behav Neurosci* 7:96
- Savanthrapadian S, Meyer T, Elgueta C, Booker SA, Vida I, Bartos M (2014) Synaptic properties of SOM- and CCK-expressing cells in dentate gyrus interneuron networks. *J Neurosci* 34:8197–8209
- Scharfman HE (1991) Dentate hilar cells with dendrites in the molecular layer have lower thresholds for synaptic activation by perforant path than granule cells. *J Neurosci* 11:1660–1673
- Scharfman HE (2018) Advances in understanding hilar mossy cells of the dentate gyrus. *Cell Tissue Res* 373:643–652
- Scharfman HE, Myers CE (2013) Hilar mossy cells of the dentate gyrus: A historical perspective. *Front Neural Circuit* 6:106
- Scharfman HE, Myers CE (2016) Corruption of the dentate gyrus by “dominant” granule cells: Implications for dentate gyrus function in health and disease. *Neurobiol Learn Mem* 129:69–82
- Schmidt B, Marrone DF, Markus EJ (2012) Disambiguating the similar: the dentate gyrus and pattern separation. *Behav Brain Res* 226:56–65
- Schmidt-Hieber C, Bischofberger J (2010) Fast sodium channel gating supports localized and efficient axonal action potential initiation. *J Neurosci* 30:10233–10242
- Schmidt-Hieber C, Jonas P, Bischofberger J (2007) Subthreshold dendritic signal processing and coincidence detection in dentate gyrus granule cells. *J Neurosci* 27:8430–8441
- Shimazaki H, Shinomoto S (2010) Kernel bandwidth optimization in spike rate estimation. *J Comput Neurosci* 29:171–182
- Sloviter RS (1991) Permanently altered hippocampal structure, excitability, and inhibition after experimental status epilepticus in the rat: the “dormant basket cell” hypothesis and its possible relevance to temporal lobe epilepsy. *Hippocampus* 1:41–66
- Sloviter RS (1994) The functional organization of the hippocampal dentate gyrus and its relevance to the pathogenesis of temporal lobe epilepsy. *Ann Neurol* 35:640–654
- Sloviter RS, Lømo T (2012) Updating the lamellar hypothesis of hippocampal organization. *Front Neural Circuit* 6:102
- Solages De C, Szapiro G, Brunel N, Hakim V, Isope P, Buisseret P, Rousseau C, Barbour B, Lna C (2008) High-frequency organization and synchrony of activity in the purkinje cell layer of the cerebellum. *Neuron* 58:775–788
- Squire L (1987) *Memory and Brain*. Oxford University Press, New York
- Su L, Chang CJ, Lynch N (2019) Spike-based winner-take-all computation: Fundamental limits and order-optimal circuits. *Neural Comput* 31:2523–2561
- Trapp P, Echeveste R, Gros C (2018) E-I balance naturally emerges from continuous Hebbian learning in autonomous neural networks. *Sci Rep* 8:8939
- Treves A, Rolls ET (1991) What determines the capacity of autoassociative memories in the brain? *Network* 2:371–397
- Treves A, Rolls ET (1992) Computational constraints suggest the need for two distinct input systems to the hippocampal CA3 network. *Hippocampus* 2:189–199
- Treves A, Rolls ET (1994) Computational analysis of the role of the hippocampus in memory. *Hippocampus* 4:374–391
- Wang XJ (2010) Neurophysiological and computational principles of fscortical rhythms in cognition. *Physiol Rev* 90:1195–1268
- Wang Y, Zhang X, Xin Q, Hung W, Florman J, Huo J, Xu T, Xie Y, Alkema MJ, Zhen M, Wen Q (2020) Flexible motor sequence generation during stereotyped escape responses. *eLife* 9: e56942
- West MJ, Slomianka L, Gundersen HJ (1991) Unbiased stereological estimation of the total number of neurons in the subdivisions of the rat hippocampus using the optical fractionator. *Anat Rec* 231:482–497
- Willshaw D, Buckingham J (1990) An assessment of Marr’s theory of the hippocampus as a temporary memory store. *Phil Trans R Soc Lond B* 329:205–215
- Yassa MA, Stark CEL (2011) Pattern separation in the hippocampus. *Trends Neurosci* 34:515–525
- Yim MY, Hanuschkin A, Wolfart J (2015) Intrinsic rescaling of granule cells restores pattern separation ability of a dentate gyrus network model during epileptic hyperexcitability. *Hippocampus* 25:297–308

Publisher’s Note Springer Nature remains neutral with regard to jurisdictional claims in published maps and institutional affiliations.